

Article

Dissolution of the Primary γ' Precipitates and Grain Growth during Solution Treatment of Three Nickel Base Superalloys

Karen Alvarado ¹, Ilusca Janeiro ¹, Sebastian Florez ¹, Baptiste Flipon ¹, Jean-Michel Franchet ²,
Didier Locq ³, Christian Dumont ⁴, Nathalie Bozzolo ¹ and Marc Bernacki ^{1,*}

- ¹ Mines-ParisTech, CEMEF-Centre de Mise en Forme des Matériaux, PSL-Research University, CNRS UMR 7635, 06904 Sophia Antipolis, France; karen.alvarado@mines-paristech.fr (K.A.); ilusca.soares_janeiro@mines-paristech.fr (I.J.); sebastian.florez@mines-paristech.fr (S.F.); baptiste.flipon@mines-paristech.fr (B.F.); nathalie.bozzolo@mines-paristech.fr (N.B.)
- ² SafranTech-Materials & Process Department, Safran SA, 78771 Magny-Les-Hameaux, France; jean-michel.franchet@safrangroup.com
- ³ Onera-DMAS, Université Paris-Saclay, 92322 Châtillon, France; didier.locq@onera.fr
- ⁴ Aubert & Duval, Département R&D Transformations, BP1, 63770 Les Ancizes, France; christian.dumont@eramet.com
- * Correspondence: marc.bernacki@mines-paristech.fr

Abstract: Second phase particles (SPP) play an essential role in controlling grain size and properties of polycrystalline nickel base superalloys. The understanding of the behavior of these precipitates is of prime importance in predicting microstructure evolutions. The dissolution kinetics of the primary γ' precipitates during subsolvus solution treatments were investigated for three nickel base superalloys (*René 65*, *AD730* and *N19*). A temperature-time codependency equation was established to describe the evolution of primary γ' precipitates of each material using experimental data, the *Thermo-Calc* software and the Johnson–Mehl–Avrami–Kolmogorov (JMAK) model. The dissolution kinetics of precipitates was also simulated using the level-set (LS) method and the former phenomenological model. The precipitates are represented using an additional LS function and a numerical treatment around grain boundaries in the vicinity of the precipitates is applied to reproduce their pinning pressure correctly. Thus, considering the actual precipitate dissolution, these simulations aim to predict grain size evolution in the transient and stable states. Furthermore, it is illustrated how a population of Prior Particle Boundaries (PPB) particles can be considered in the numerical framework in order to reproduce the grain size evolution in the powder metallurgy N19 superalloy. The proposed full-field strategy is validated and the obtained results are in good agreement with experimental data regarding the precipitates and grain size.

Keywords: grain growth; Smith–Zener pinning; level-set; full-field simulations; superalloys; dissolution kinetics



Citation: Alvarado, K.; Janeiro, I.; Florez, S.; Flipon, B.; Franchet, J.-M.; Locq, D.; Dumont, C.; Bozzolo, N.; Bernacki, M. Dissolution of the Primary γ' Precipitates and Grain Growth during Solution Treatment of Three Nickel Base Superalloys. *Metals* **2021**, *11*, 1921. <https://doi.org/10.3390/met11121921>

Academic Editor: Chang Yong Jo

Received: 29 September 2021

Accepted: 24 November 2021

Published: 28 November 2021

Publisher's Note: MDPI stays neutral with regard to jurisdictional claims in published maps and institutional affiliations.



Copyright: © 2021 by the authors. Licensee MDPI, Basel, Switzerland. This article is an open access article distributed under the terms and conditions of the Creative Commons Attribution (CC BY) license (<https://creativecommons.org/licenses/by/4.0/>).

1. Introduction

In polycrystalline nickel base superalloys, the γ' phase is found in several types of precipitates that can basically be distinguished based on their size and specific role in the microstructure. The so-called primary precipitates are the largest ones, typically a few microns (μm). Secondary and tertiary ones are much finer and essentially control the mechanical behavior [1–3]. After forging operations, polycrystalline γ - γ' superalloys are submitted to partial solution treatment, thus below the γ' solvus temperature (T_{solvus}), where primary γ' precipitates are kept to avoid excessive grain growth (GG), while the fine hardening precipitates dissolved to reprecipitate again with an optimized size distribution during the subsequent controlled cooling.

Primary γ' precipitates control the grain size by hindering grain boundary (GB) motion through the Smith–Zener pinning (SZP) mechanism [4–7]. In order to properly control the

grain size during a specific subsolvus solution treatment, the evolution of these primary precipitates as a function of time and temperature must be understood.

The dissolution of primary γ' precipitates in nickel base superalloys has mainly been studied experimentally [1,8–12] but not so much in full-field numerical works [13–15] at the polycrystalline scale.

Such simulations may help clarify, predict, and control microstructure evolution when precipitate dissolution occurs during heat treatments (HT), at subsolvus and near-solvus temperatures for each considered material. In the present work, only the effect of primary γ' precipitates will be considered, as secondary and tertiary ones are dissolved during subsolvus solution treatments.

The full-field models are of great interest as they can reproduce microstructure evolutions and heterogeneities. Several methods have been developed to reproduce the SZP mechanism at the polycrystalline scale, considering the presence of second phase particles (SPP) in the microstructure. For instance, probabilistic methods such as the Monte Carlo (MC) or Pott's model [16–19] and the Cellular Automata (CA) models [20,21] were used to account for SZP. More complex models have been developed in the last decades, such as the Front-Tracking methods [22], and the Front-Capturing approaches, including the multi phase-field (MPF) [23–30] and level-set (LS) [13,31–33] frameworks.

All these full-field approaches can integrate SPP into their formulation. A spherical shape to describe them is commonly adopted, although the influence of more complex shapes has also been investigated [28,31,34]. In some cases, real precipitate morphology, obtained from Electron BackScatter Diffraction (EBSD) maps, secondary electron (SE) images [31,32] or backscattered electron (BSE) images [31], has been used. However, all these works consider the precipitates as static objects. This reasoning is valid at low temperature (relatively to T_{solvus}) where precipitates do not evolve (or very slowly) or at high temperature where precipitates dissolve very fast, in which case SZP does not need to be modeled at all. However, at a temperature just below T_{solvus} , precipitate dissolution and grain growth can be concomitant. Moreover, the Ostwald ripening mechanism can also take place at long annealing times.

For high temperatures close to T_{solvus} , the precipitate volume fraction and size distribution can evolve significantly at the same timescale of recrystallization and GG phenomena, which motivates this work focused on GG, where the SZP plays a role of prime importance.

The SZP-GG coupling exhibits complex behaviors [9,31,35] that include precipitate evolution. To our knowledge, few numerical works consider the precipitate evolution, some of them using the PF method [30,36] and other using the LS approach [13]. This work adopts the LS approach presented in [13], where a special treatment at the precipitate/GB interface is made to model incoherent precipitates (i.e., assuming the precipitate/GB contact angle to be 90°).

The studied materials are presented in Section 2 as well as the experimental methods used to get data regarding the evolution of precipitates and matrix grains during annealing at different temperatures and times. A phenomenological model is then established in Section 3 for describing the evolution of precipitate area fraction and size as a function of time and temperature by combining Thermo-Calc simulations and a JMAK model [11,12]. Section 3 also presents how the parameters which will be used for describing GB motion in the subsequent full-field simulations have been obtained from the experimental grain growth kinetics. Both the phenomenological model for precipitate evolution and GB motion parameters are then used in full-field simulations conducted within an LS framework. Section 4 introduces the LS method and the required numerical treatment for considering precipitate evolution as a function of the dissolution velocity. The results of the LS full-field simulations are presented in Section 5 and compared with the experimental data for validation. The last section summarizes the conclusions and opens perspectives for further works.

2. Materials and Methods

Three nickel base superalloys, *René 65*, *AD730* and *N19*, were submitted to heat treatments to study the dissolution kinetics of primary γ' precipitates. Table 1 shows their chemical compositions. These are materials of high technological interest as they are candidates for high temperature applications in aeronautical components, where strict grain size criteria must be fulfilled.

Table 1. Chemical composition of the used billets of *René 65* [37], *AD730* [38] and *N19* [39] superalloys (wt.%).

Superalloy	Ni	Cr	Co	Ti	Al	Mo	W	Fe	Nb	Zr	B	C	Hf
<i>René65</i>	Bal.	16	13	3.7	2.1	4	4	1	0.7	0.05	0.016	0.01	-
<i>AD730</i>	Bal.	15.7	8.5	3.4	2.25	3.1	2.7	4	1.1	0.03	0.01	0.015	-
<i>N19</i>	Bal.	12.9	11.8	3.8	2.5	4.7	3.2	-	1.6	0.06	0.015	0.022	0.3

2.1. As-Received States

The initial (“as-forged”) state of the samples studied in this work come either from a conventional cast-and-wrought process (for *AD730* and *René 65*) or from a powder metallurgy route and isothermal forging (for the *N19*). Figure 1 illustrates the initial microstructure of each alloy. Images on the left with low magnification show the distribution of the primary γ' precipitates in the microstructure. The images on the right present the morphology of primary and secondary γ' populations. The initial microstructures show noticeable differences, even between *AD730* and *René 65* alloys, which have quite similar chemical compositions and are both cast-and-wrought alloys. This highlights the importance of the thermomechanical background on the fraction and distribution of γ' precipitates in the microstructure. The presence of secondary and tertiary precipitates in the microstructure is notably determined by the last cooling undergone by the material, but they will be dissolved again at the targeted temperature in this work.

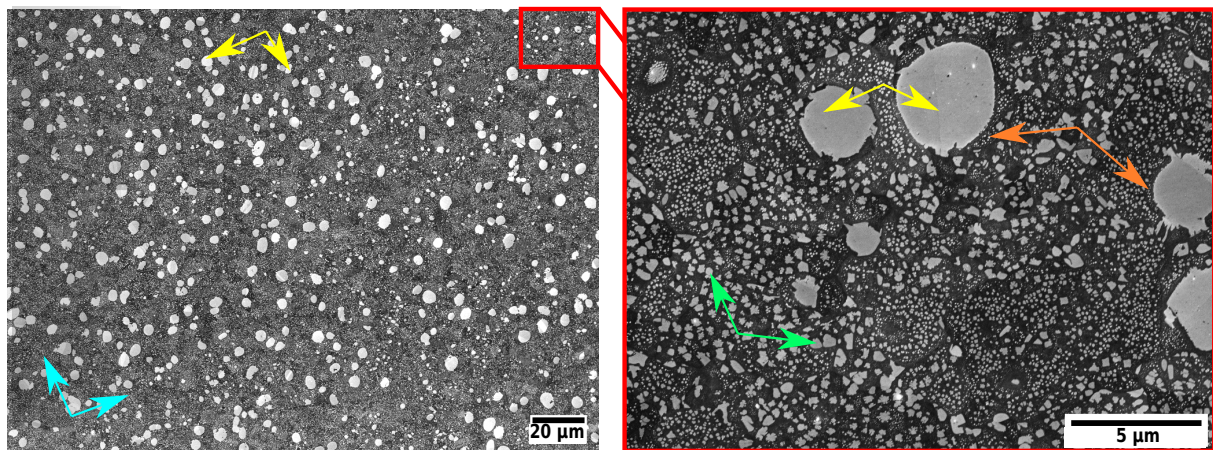
2.1.1. Thermo-Calc Simulations and Experimental Data

Thermo-Calc software (TCNI9 database, Thermo-Calc, Stockholm, Sweden) [40] was used to estimate the γ' phase volume fraction of each superalloy as a function of temperature by using the TCNI9 database and the compositions given in Table 1. Figure 2 presents the volume fraction of γ' phase as a function of temperature for the three alloys. The γ' volume fraction estimated at room temperature was calculated as 37% for *René 65* and *AD730* and 43% for *N19*, which are in agreement with the values presented in the literature [38,41,42]. According to the curves in Figure 2, the full γ' phase dissolution temperatures (T_{solvus}) estimated by *Thermo-Calc* correspond to 1093 °C, 1108 °C and 1138 °C for *René 65*, *AD730* and *N19*, respectively.

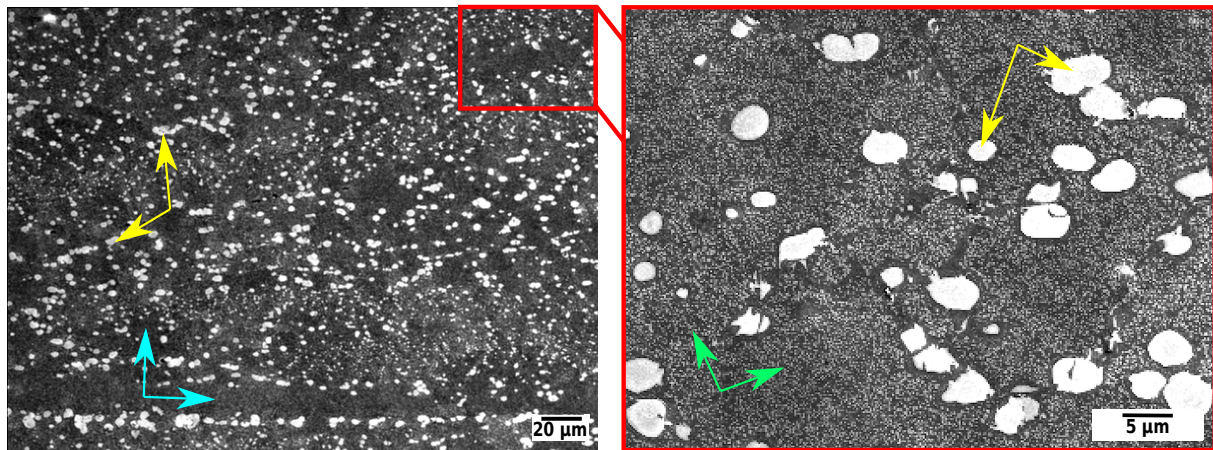
2.2. Methods

Heat treatments were performed at different times and temperatures for all three materials (summarized in Table 2), followed by cooling at 100 °C/min or water quenching. The evolution of primary γ' precipitates was considered to be negligible during cooling at 100 °C/min, as confirmed by comparison with the primary γ' evolution obtained after water quenching.

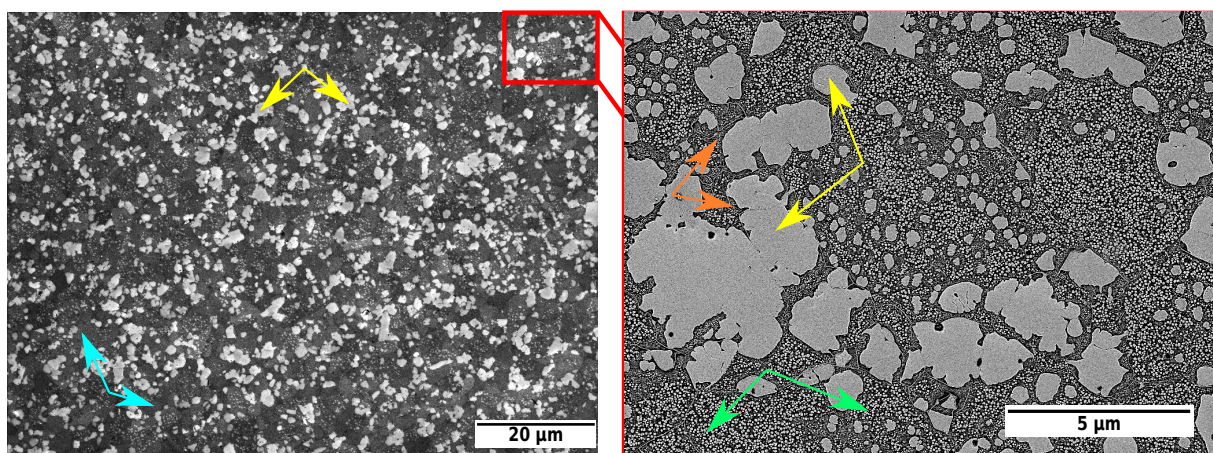
Sample preparation for microstructure analysis was carried out in two different ways to obtain high-contrast images between the γ matrix and the γ' precipitates. The first preparation protocol was a mechanical polishing down to 1 μm grid and then electrolytic polishing with a solution of 10% perchloric acid and 90% methanol at 10 °C, under 35 V for 5–8 s. The second was a mechanical polishing down to 0.25 μm grid and etching (with citric acid or *HCl/CH₃COOH*).



a. René 65



b. AD730



c. N19

→ γ Matrix → Primary γ' → Secondary γ' → Tertiary γ'

Figure 1. Secondary electron images of the initial (“as-forged”) microstructures at two different magnifications for (a) René 65; (b) AD730 and (c) N19 superalloys.

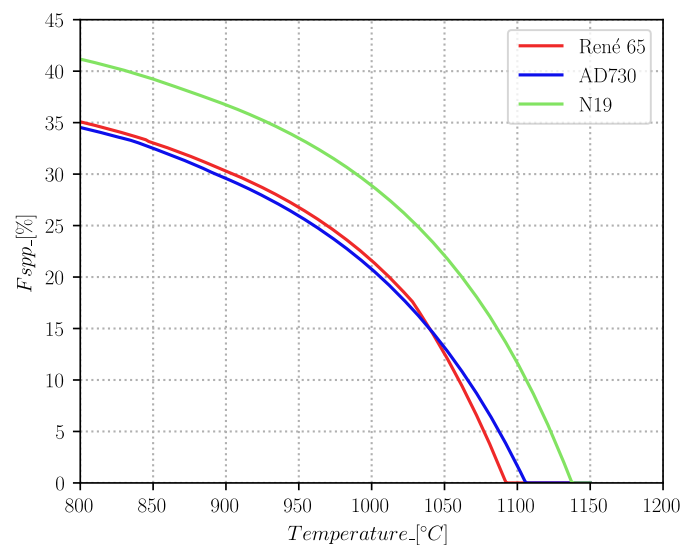


Figure 2. γ' phase volume fraction vs. temperature curves for the René 65, AD730 and N19 superalloys (obtained from Thermo-Calc calculations).

Microstructural analysis was performed with two microscopes. The samples that received the first protocol were examined using the secondary electron detector (SE) of a Zeiss Supra40 Scanning Electron Microscope (SEM) (Zeiss, Oberkochen, Germany).

SE images were acquired with an acceleration voltage of 3 kV, at 3–5 mm working distance and with 60 μm diaphragm size. The samples prepared with the second protocol were examined by optical microscopy. Ten images of 100 μm \times 75 μm (for AD730 and N19) and 227 μm \times 170 μm (for René 65) were taken for each sample for the sake of statistical representativity. In addition, 350–400 precipitates/image were found in René 65 microstructure after annealing at temperatures below 1050 $^{\circ}\text{C}$, i.e., 60 $^{\circ}\text{C}$ below T_{solvus} . The higher the annealing temperature, the lower the number of precipitates found, reaching 140–230 precipitates/image at 1090 $^{\circ}\text{C}$. The same behavior was observed in AD730 and N19 alloys images, where the number of precipitates decreases as the temperature increases. *ImageJ* software (1.52a, LOCI, University of Wisconsin, Madison, WI, USA) [43] was used for image binarization and quantitative analysis of the γ' phase area fraction and average precipitate size.

EBSM maps were acquired with an acceleration voltage of 20 kV, at 15–16 mm working distance, and 120 μm diaphragm size. They were analyzed with MTEX [44], an open MATLAB toolbox (R2017a, MathWorks, Natick, MA, USA). A GB was defined when the disorientation between two neighboring points exceeded 10 $^{\circ}$. Regarding the γ' phase identification, it cannot be done with EBSM data because this phase is indistinguishable from the γ matrix [45] because of their crystallographic structure being too close to each other. Therefore, in the case of AD730, a size criterion has been applied to separate the particles from the grains. The particles with $0.3 \mu\text{m} \leq D_{spp} \leq 4 \mu\text{m}$ were considered as γ' primary precipitates. The step size of the maps was adapted; as the annealing temperature increased, the grains became larger and larger. For instance, for the 4 h HT at 1070 $^{\circ}\text{C}$, an EBSM map of size 1130 μm \times 840 μm with a step size of 1.13 μm was analyzed, giving a total number of 5120 grains. For the 4 h HT at 1100 $^{\circ}\text{C}$, two EBSM maps were taken to reach a good statistical representativity of the sample; the size of the maps was 2180 μm \times 1700 μm with a step size of 4 μm , and they included a total number of 2272 grains.

For the N19 material, it was not possible to distinguish the primary γ' precipitates from the grains (γ phase) with the same strategy because the primary γ' precipitates have a size similar to that of the grains. Therefore, EBSM analysis was coupled with energy dispersive X-ray (EDS) analysis [46] to distinguish the two phases based on their chemical compositions. However, one drawback of this technique is that the spatial resolution of the EDS is limited to about 0.5 μm under the current acquisition setup. For these EBSM

analyses, two maps of size $120\ \mu\text{m} \times 90\ \mu\text{m}$ with a $step = 0.08\ \mu\text{m}$ were analyzed, giving a total number of around 1600 grains for the samples annealed at $1110\ ^\circ\text{C}$ and 1200 grains at $1130\ ^\circ\text{C}$.

Table 2. Heat treatments done for each superalloy (a) *René 65*; (b) *AD730* and (c) *N19*.

(a)											
René 65 Heat Treatments											
Domain	Temperature [°C]	Holding Time [min]									
		5	25	90	240						
Subsolvus	1010									×	
	1030									×	
	1050									×	
	1065					×		×		×	
	1090					×				×	
	1100									×	
Solvus	1110				×		×			×	
Supersolvus	1115									×	
	1120									×	
	1125									×	
	1130									×	
	1140									×	
(b)											
AD730 Heat Treatments											
Domain	Temperature [°C]	Holding Time [min]									
		10	15	20	30	60	240				
Subsolvus	1060	×			×			×		×	
	1070	×			×			×		×	
	1080	×			×			×		×	
	1090	×			×			×		×	
	1100										
Solvus	1110	×			×				×	×	
Supersolvus	1120						×				
	1125						×				
	1140	×		×			×		×		
	1150	×			×		×				
	1160	×		×	×		×		×		
(c)											
N19 Heat Treatments											
Domain	Temperature [°C]	Holding Time [min]									
		1	2	3	10	20	30	60	120	240	
Subsolvus	1110				×			×		×	×
	1120				×			×			×
	1130				×	×	×	×			×
	1140				×	×		×			×
Solvus	1150	×	×		×	×	×	×	×	×	
Supersolvus	1160	×	×		×	×			×	×	
	1180	×		×	×	×			×	×	

3. Experimental Grain Size and Precipitate Evolution Kinetics

3.1. Area Fraction of Primary γ' Precipitates after Annealing for 4 h

Figure 3 shows micrographs after the four-hour isothermal HT carried out at different temperatures for each alloy. Note that the γ' precipitates of each alloy have different morphologies, being directly related to the previous thermomechanical treatments. However, a common point is the dissolution process itself, which is the reduction of the volume fraction of primary γ' precipitates with increasing temperature. In addition, as is visible from the crystallographic contrast of some images, the primary γ' dissolution leads to an increase in the grain size (Figure 3b,c, for instance).

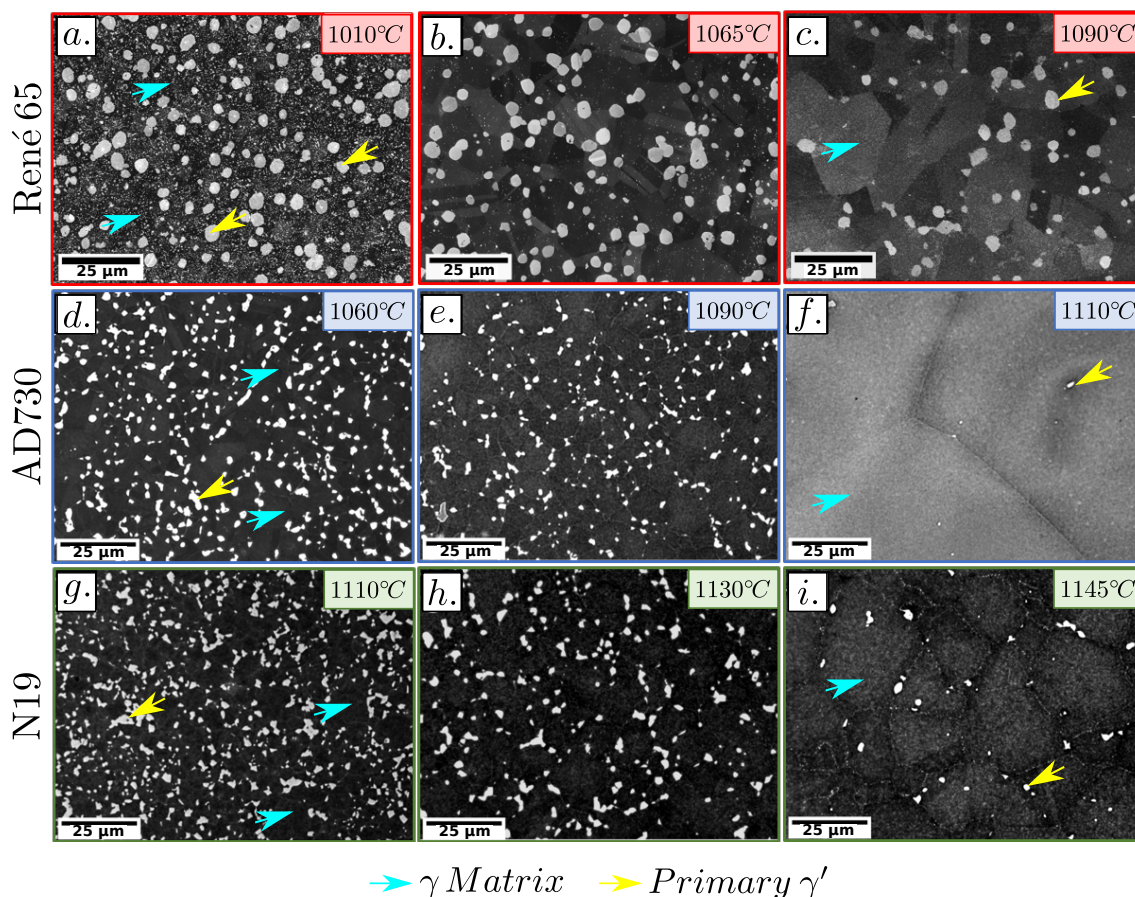


Figure 3. SEM SE micrographs obtained using the first preparation protocol after 4 h heat treatment for *René 65* at (a) 1010 °C; (b) 1065 °C; (c) 1090 °C; for *AD730* at (d) 1060 °C; (e) 1090 °C; (f) 1110 °C and optical images obtained using the second preparation protocol for *N19* at (g) 1110 °C; (h) 1130 °C and (i) 1145 °C (*N19*). Bright particles are the primary γ' -phase precipitates undissolved during annealing.

The smaller the primary γ' fraction in the microstructure, the larger the average grain size. This result has already been proven numerous times in different alloys [2,6,41,47–49] and can be explained by the SZP phenomenon.

Figure 4 shows the evolution of γ' phase fraction as a function of T . The primary γ' fraction significantly evolves (dissolution mechanism) when the temperature is close to the solvus temperature ($50\text{ °C} - T_{\text{solvus}} \leq T \leq T_{\text{solvus}}$), and remains constant when the temperature is far from the solvus point, as illustrated in Figure 4a,c. The presence of secondary and tertiary γ' precipitates was not considered in the measurement of the γ' phase fraction. However, they are given reminders on these graphs with labels γ'_{II} and γ'_{III} , respectively. An experimental or effective T_{solvus} could be determined as the temperature at which the area fraction of primary γ' is equal to zero after 4 h isothermal holding. Figure 4 also exhibits a comparison between the *Thermo-Calc* curves and the experimental data.

Note that thermodynamic simulation values do not match exactly with the experimental T_{solvus} obtained for the René 65 and N19 alloys. For temperatures close to T_{solvus} , the *Thermo-Calc* curve and the experimental points seem to follow the same evolution and shape. For the AD730 alloy (Figure 4b), there is a much better fit between experimental points and the *Thermo-Calc* results; however, for the other two alloys (Figure 4a,c), there is a slight offset. A shift of the *Thermo-Calc* curve was done to find a better fit with the experimental points, an offset of 17 °C and 12 °C were applied to the René 65 and N19 alloys, respectively. From these results, it was defined that the effective T_{solvus} values for 4 h annealing corresponds to 1110 °C, 1108 °C and 1150 °C for the René 65, AD730 and N19 superalloys, respectively.

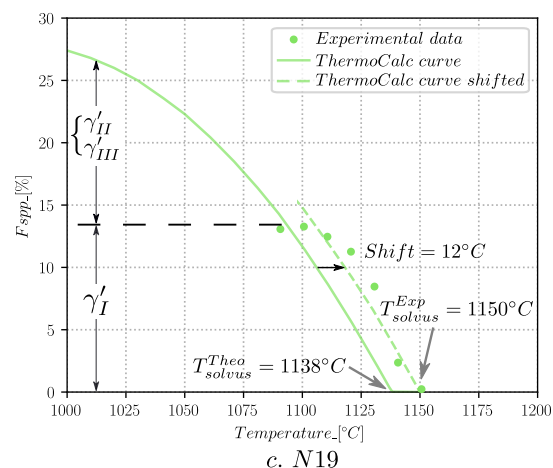
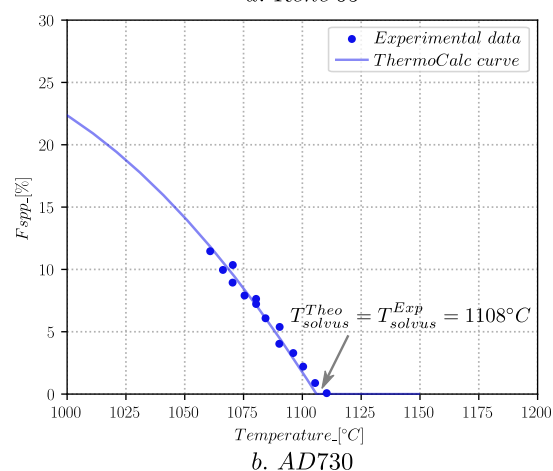
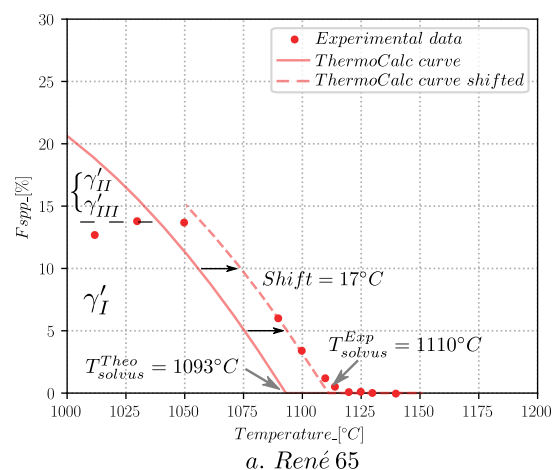


Figure 4. γ' area fraction after 4 h annealing treatment as a function of temperature for alloys (a) René 65; (b) AD730 and (c) N19.

The shifted curves can be described as a function of $T - T_{solvus}$ difference, as presented in Figure 5. The same curve can then be used to reproduce the experimental behavior of the *René 65* and *AD730*, for temperatures in the 50 °C range below the T_{solvus} . This shows that the overall area fraction evolution is similar for both conventional forged materials at the equilibrium state.

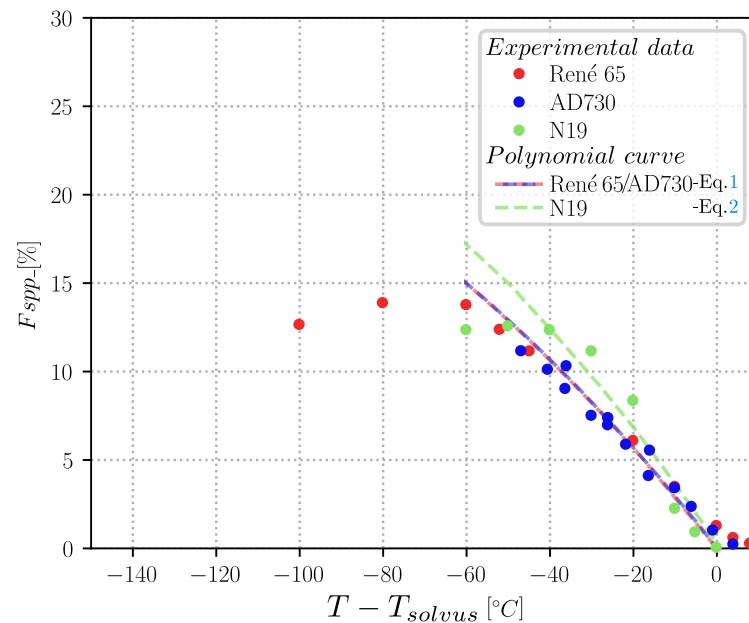


Figure 5. Area fraction of primary γ' precipitates after a four-hour isothermal treatment and the respective curves obtained through phenomenological fits established on the shape of the *Thermo-Calc* curves (described in Equations (1) and (2)).

The dissolution kinetics, i.e., the slope of the curve, for the *N19* is steeper compared to the *René 65* and *AD730* alloys. This result is physically relevant as the annealing temperatures and T_{solvus} are higher for this alloy. The equations, i.e., phenomenological models that describe the behavior presented in Figure 5 are Equation (1) for *René 65* and *AD730* alloys and Equation (2) for *N19*; they were obtained as second order polynomial approximations of the shifted curves:

$$f_{spp_{eq}René\ 65/AD730}(T) = -0.00084(T - T_{solvus})^2 - 0.3(T - T_{solvus}), \quad (1)$$

$$f_{spp_{eq}N19}(T) = -0.001(T - T_{solvus})^2 - 0.35(T - T_{solvus}), \quad (2)$$

where $f_{spp_{eq}}$ is the equilibrium volume fraction considered to be reached after 4 h and actually corresponds to the measured primary γ' precipitate fraction as secondary and tertiary precipitates are already dissolved at about 50 °C below the solvus point. The shape of the shifted curves, as well as the values of the obtained second order coefficients, illustrates that linear approximations, although less precise, would be acceptable.

3.2. Area Fraction of Primary γ' Precipitates as a Function of Time and Temperature

The main purpose of this part is to establish a model that can predict the area fraction of the primary γ' phase as a function of time and temperature within the 50 °C window below T_{solvus} . Through experimental data and *Thermo-Calc*, two equations that reproduce the fraction of primary γ' as a function of temperature were obtained in Section 3.1 (Equations (1) and (2)). A JMAK model was then used to describe the diffusion-controlled dissolution of spherical precipitates. This relation has already been used in several works to

represent the dissolution of γ' phase for polycrystalline nickel base superalloys [11,12,50], as follows:

$$f_{spp}(t, T) = f_{eq}(T) + (f_0 - f_{eq}(T)) \cdot \exp\left(\frac{-t}{t_1}\right). \quad (3)$$

The area fraction of precipitates at thermodynamic equilibrium is represented by f_{eq} , f_0 corresponds to the primary γ' area fraction at $t = 0$ s (as-received material) and t_1 is a time-dependent constant.

Assuming that Equation (3) is valid to describe the γ' phase dissolution of the three alloys, and that Equations (1) and (2) are valid over the range $50 - T_{solvus} \leq T \leq T_{solvus}$ to provide the equilibrium area fraction of primary γ' precipitates ($f_{spp,eq,alloy} = f_{eq}$), the following expression is obtained:

$$f_{spp}(t, T) = f_{spp,eq,alloy}(T) + (f_0 - f_{spp,eq,alloy}(T)) \cdot \exp\left(\frac{-t}{t_1}\right). \quad (4)$$

This time dependent model was validated through several heat treatments ranging from 10 min to 4 h at different temperatures for each of the three studied alloys. The initial primary precipitates area fraction f_0 and the identified value of the t_1 constant were respectively 12.5% and 1300 s for René 65 and AD730 and 18.5% and 250 s for N19. It is worth mentioning that the constant t_1 , once identified for the best fit of one curve (one temperature), is in fact quite precise for all temperatures in the analyzed range, contrary to the work presented in [11], where the parameter t_1 needs to be identified for each temperature.

Figure 6 shows a good agreement between the experimental results and Equation (4) model predictions. The evolution of the γ' phase area fraction could then be described in the considered range of time and temperature. A few data available for the René 65 alloy have also been added on the plot of Figure 6a.

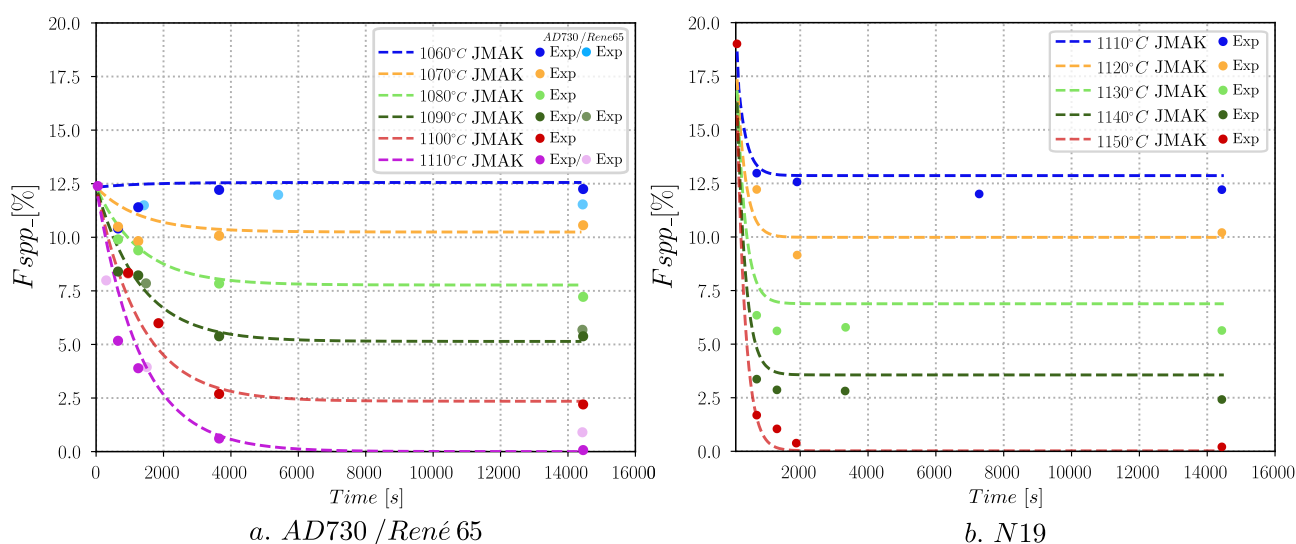


Figure 6. Comparison between the phenomenological model Equation (4) (dashed lines) and experimental results (points) of the primary γ' fraction at different times and temperatures for (a) René 65 and AD730 and (b) N19 superalloys.

3.3. Primary γ' Precipitate Size Evolution

Figure 7 illustrates the evolution of the mean primary precipitate size (\bar{D}_{spp}) for the three alloys. During short annealing times, the average precipitate size decreases, as could be expected from the dissolution process. However, after 1 h of heat treatment, a slight increase in the mean size of the precipitate can be seen. This behavior suggests the presence of the Ostwald ripening phenomenon, for which large precipitates grow and the small ones shrink and disappear, while keeping the particle fraction constant. The driving force

of this mechanism is the minimization of interfacial energy (Gibbs Thomson effect). A composition gradient in the matrix between precipitates of different curvature radii induces a diffusion flux from the small precipitates towards the large ones leading to the shrinkage and disappearance of small precipitates and eventually to a decrease of the free energy associated with the overall matrix–precipitate interface area.

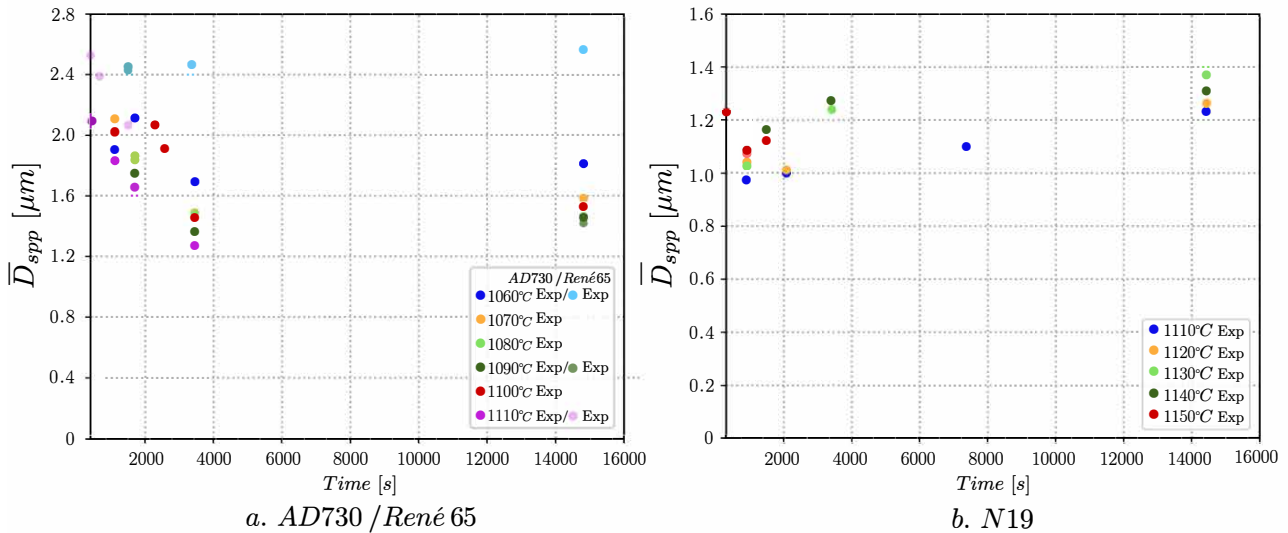


Figure 7. Mean precipitate size in the (a) AD730/René 65 and (b) N19 superalloys.

3.4. Precipitate Dissolution Rate Derived from the JMAK Model

The precipitate area fraction as a function of time and temperature has already been established using a JMAK model given by Equation (3) where the precipitate area fraction is described as a function of the initial and the equilibrium fractions.

The precipitate dissolution rate v_{spp} (defined here as the rate at which the precipitate interface moves) can then be described using the following relation:

$$v_{spp}(t, T) = \frac{S}{2\pi\bar{r}_{spp}(t, T)N_{spp}(t, T)} \frac{df_{eq}(T)}{dt} = -\frac{S}{2\pi\bar{r}_{spp}(t, T)N_{spp}(t, T)} \frac{f_1}{t_1} \cdot \exp\left(-\frac{t}{t_1}\right), \quad (5)$$

with S the total considered area, $\bar{r}_{spp}(t, T)$ the arithmetic mean precipitate radius and $N_{spp}(t, T)$ the remaining number of precipitates (at each step of the simulations). This velocity expression will be introduced later in the full-field simulations to reproduce the precipitate interface velocity observed experimentally.

3.5. Grain Size Evolution

Figure 8a illustrates the evolution of the experimental arithmetic mean grain size for the AD730 and René 65 alloys. The grain size does not change significantly when the annealing is performed at a temperature far from T_{solvus} , as the grains are blocked by the rather high γ' phase fraction present in the initial material (12.5%). However, for higher temperatures (>1080 °C), where the dissolution of the precipitates is more significant, the grains may grow more and more, especially when the microstructure is free from precipitates (at $T_{solvus} = 1110$ °C).

For the N19 alloy (Figure 8b), a similar behavior is observed, with only slight grain growth at temperatures far below T_{solvus} . However, for temperatures close to T_{solvus} , a very significant evolution is noted in the first minutes, but after 1 h heat-treatment, the average grain size tends to keep the same value. The N19 superalloy behavior is thus different from that of the AD730 for temperatures close to the solvus domain. It will be

necessary to understand why the mean grain size of this PM material behaves differently and then considers this effect in the simulations to compare the experimental data with the numerical results.

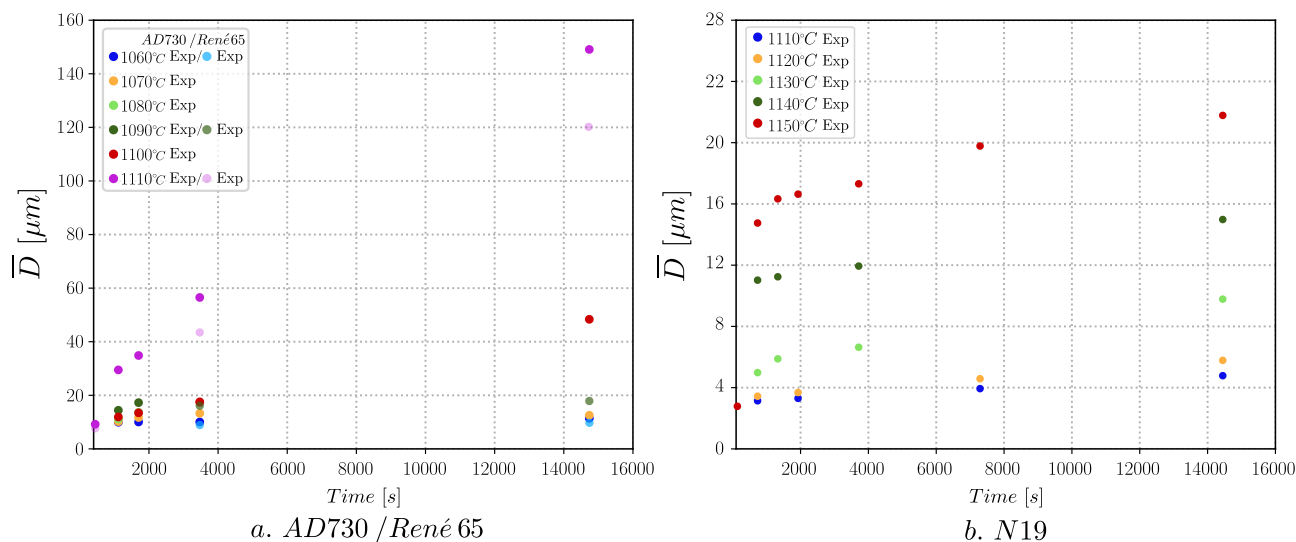


Figure 8. Mean grain size after subsolvus heat-treatments for (a) AD730/René 65 for (b) N19 superalloys.

3.6. Experimental Data Used for the Identification of GB Migration Parameters

The procedure used to obtain the values of the GB migration parameters consistent with the experimental data for each material is presented below. This identification is mandatory for the forthcoming comparison between the experimental data and the numerical results.

The main parameter controlling the migration of a GB submitted to a driving force is its mobility, which can be approximated through an Arrhenius law as follows:

$$M(T) = M_0 \exp\left(\frac{-Q_m}{RT}\right), \quad (6)$$

with M_0 a pre-exponential factor considered to be constant, Q_m the activation energy for GB migration, T the absolute temperature, and R the gas constant. Here, the mobility is considered to be the same for all GB, independently of crystallographic properties. The values of M , M_0 and Q_m can be obtained from the experimental GG data when there are no precipitates present in the material to hinder GB motion, i.e., at the supersolvus domain.

The procedure used to calculate M_0 and Q_m (Equation (6)) can be summarized by the following steps [51]:

1. Supersolvus heat treatments were performed at different temperatures for several holding times for the AD730, up to 50 °C above the T_{solvus} and for the N19 material, up to 30 °C above T_{solvus} as presented in Figure 9. It can be noticed again here in the supersolvus domain that the grain size of the N19 alloy stagnates at about 20 μm , whereas the grain size of the two other alloys keeps increasing with time and temperature.
2. A first approximation of the reduced mobility ($M\gamma_{BT}$) is obtained for each temperature by the best fit of the experimental data with a Burke & Turnbull law (B&T) [52]:

$$\bar{R}^2 - \bar{R}_0^2 = \frac{1}{2}(M\gamma)_{BT}t. \quad (7)$$

with γ the grain boundary energy set here and in the following to 0.6 J/m², which corresponds to GB energy in pure nickel at 1000 °C [53].

3. As the reduced mobility ($M\gamma$) is actually model-dependent [51], these values will have to be further refined based on full-field simulations as described in Sections 5.1.1 and 5.2.1.

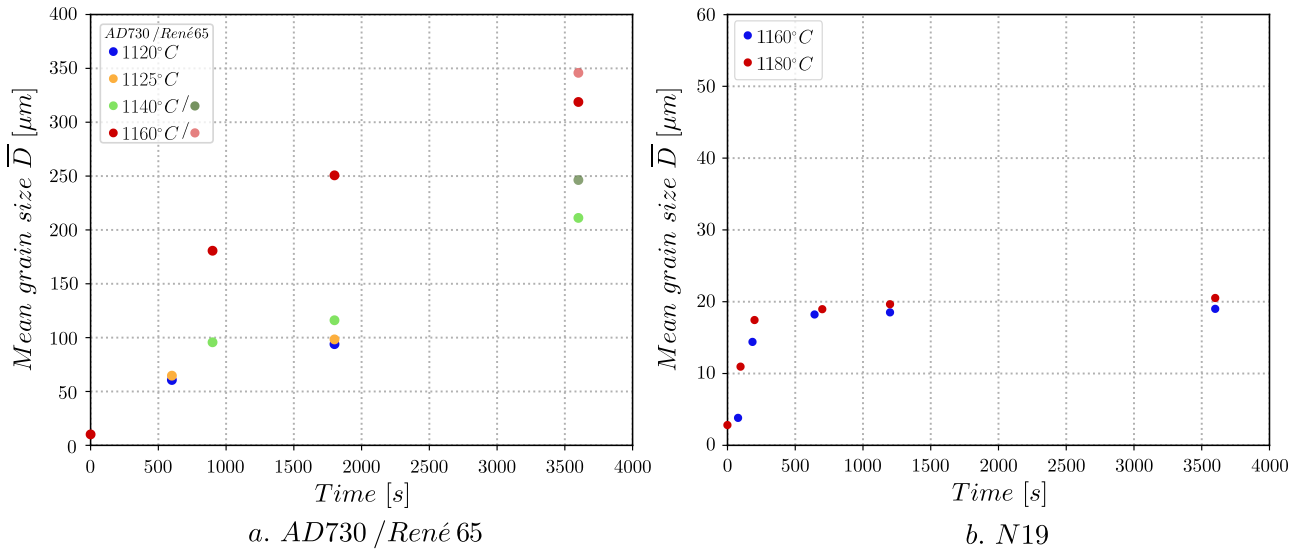


Figure 9. Grains mean size after supersolvus heat treatments for (a) AD730/René 65 and for (b) N19 superalloys.

4. Full-Field Model Description

In the following, the LS method is used to perform *full-field* GG simulations under the influence of the primary γ' precipitates submitted to dissolution as described with the formerly established phenomenological model. First, the global numerical framework is introduced below.

4.1. Level-Set Approach to Simulate GG

In this approach, each grain G (sub-domain) of the calculation domain Ω (polycrystal) can be defined by computing a signed Euclidean distance function (φ) to its interface. This function is considered to be positive inside the grain and negative outside, and the interface (i.e., grain boundary) is then described by the zero-isovalue as follows:

$$\begin{cases} \varphi(x, t) = \pm d(x, \Gamma(t)), x \in \Omega \\ \Gamma(t) = \{x \in \Omega, \varphi(x, t) = 0\} \end{cases} \quad (8)$$

where $d(x, \Gamma(t))$ is the distance between a point x and the boundary $\Gamma(t)$ of the considered grain G . The interface migration can be deduced by the resolution of a set of convective equations, with N_G the number of grains:

$$\begin{cases} \frac{\partial \varphi_i}{\partial t} + \vec{v}_i \cdot \nabla \varphi_i = 0 \\ \varphi_i(t = 0, x) = \varphi_i^0 \quad \forall i \in \llbracket 1, N_G \rrbracket \end{cases} \quad (9)$$

When GG is studied, it is classically accepted that, at the mesoscopic scale, the behavior of φ is only driven by the curvature flow [54]. Thus, the grain boundary velocity can be approximated by:

$$\vec{v}_i = -M_i \gamma_i \kappa_i \vec{n}_i, \quad (10)$$

where M_i is the local grain boundary mobility, γ_i the local grain boundary energy, $\kappa_i = \nabla \cdot \vec{n}_i$ the local mean curvature (i.e., the curvature in 2D and the sum of the main curvatures in 3D) and $\vec{n}_i = -\frac{\nabla \varphi_i}{\|\nabla \varphi_i\|}$ the outward unitary normal vector to $\Gamma_i = \partial G_i$. Classically, by using Equation (10) and if the LS functions remain distance functions at each time step

($\|\nabla\varphi_i\| = 1$), Equation (9) can be rewritten as a set of diffusive equations [55] avoiding the exact calculation of the GB curvature:

$$\begin{cases} \frac{\partial\varphi_i}{\partial t} - M_i\gamma_i\Delta\varphi_i = 0 \\ \varphi_i(t=0, x) = \varphi_i^0 \quad \forall i \in \llbracket 1, N_G \rrbracket \end{cases} \quad (11)$$

For this work, the material is considered as isotropic, i.e., $M_i = M(T)$ is assumed to be only temperature-dependent and $\gamma_i = \gamma$ is considered as constant [56]. However, LS can also be applied to more realistic microstructures considering the heterogeneity of $M\gamma$, taking into consideration the misorientation angle [57–61], the inclination of the grain boundaries [60,62,63] and the influence of solute segregation [64].

In the considered isotropic assumption context and at a high temperature, the mobility can be approximated considering the Arrhenius law presented in Equation (6).

To summarize, the GG simulation under the effect of capillary pressure in the proposed finite element framework (FE) coupled to the LS method involves the following steps at each time increment:

- Grain boundary migration is calculated by solving Equation (11) for each active LS function. In order to limit the computational cost, a Graph coloration/recoloration technique is used [65] allowing for reducing the number of LS functions by grouping non-neighboring grains in common LS functions, called global Level-Set (GLS) functions. Each GLS contains numerous grains that are separated by a minimum distance, hence $N_{GLS} \ll N_G$ [65].
- After the resolution of Equation (11), voids or overlaps can appeared at the GB and their junctions. In order to treat this issue and remove such non-physical regions, the methodology proposed in [57] and described by Equation (12) is used for each GLS function:

$$\hat{\varphi}_i = \frac{1}{2} \left(\varphi_i - \max_{j \neq i} \varphi_j \right), \quad \forall i = 1 \dots N_{GLS}, \quad (12)$$

where $\hat{\varphi}_i$ is used as the new corrected GLS function.

- All active GLS functions are reinitialized ($\|\nabla\varphi\| = 1$) with the direct reinitialization method proposed in [66]. Indeed, one of the weaknesses of the LS formulation is to not naturally conserve the metric property of an LS function initially defined as a distance function. To ensure the validity of the diffusive form of Equation (11) and to describe curvature flow migration, distance functions are required at least near the interfaces.

Several approaches have been developed to treat the reinitialization procedure in regular grids, or unstructured FE meshes [67–69]. Here, the parallel and direct reinitialization algorithm proposed by Shakoore et al. [66] was adopted as a fast and accurate method. Discussions concerning the residual error of this approach are detailed in [70].

- The negative GLS functions (grains which have disappeared) are removed from the system of equations.
- To avoid numerical coalescence, the re-coloring technique presented in [32,65] is applied.
- Interface remeshing operations following the methodologies proposed in [31,71] are performed if required.

4.2. Description of SPP

The multiple junctions treatment based on [57] has been applied both for 2D and 3D simulations of GG in single phase materials or with static SPP using the LS approach [32,55,56,72]. A Modified Multiple Junctions Treatment (MMJT) has recently been proposed in [13] to consider the precipitates as an LS function in FE-LS GG modeling. This new description of the particles opens the possibility of making SPP evolve. The MMJT can be summarized as follows:

$$\hat{\varphi}_i(t, x) = \frac{1}{2} \left(\varphi_i(t, x) - \max \left(\max_{j \neq i} (\varphi_j(t, x)), \varphi_{spp}(t, x) \right) \right), \quad \forall i = 1 \dots N_{GLS}, \quad \forall x \in \Omega. \quad (13)$$

Without SPP, the MMJT is equivalent to the classical numerical treatment (Equation (12)). When SPP are present, it enables by successive iterations to impose the Young–Herring equilibrium for incoherent SPP (see [13] for further details).

At the beginning of the simulation, an initial mesh is generated, followed by the polycrystal creation. The latter must be statistically representative of the initial state of the studied material. Then, the grain distance functions φ_i are adjusted to introduce the new particle distance function φ_{spp} .

4.3. SPP Interface Velocity

A convective equation is considered for φ_{spp} to make the precipitate interfaces evolve. A SPP interface velocity, v_{spp} , is introduced at the SPP interfaces in order to reproduce the precipitate dissolution given by the JMAK model previously developed. More precisely, a continuous velocity field, v , is applied through the Laplacian equation Equation (14) considering Dirichlet boundary conditions [73] at the precipitate interfaces. In the end, this smoothed velocity field v is implemented to calculate the velocity \vec{v} oriented towards the center of each precipitate (see Figure 10).

$$\begin{cases} \Delta v = 0 \\ v = v_{spp} \text{ at } \Gamma_{spp} \end{cases} \quad (14)$$

and

$$\vec{v} = v \cdot \vec{n} = -v \cdot \nabla \varphi_{spp}, \quad (15)$$

with \vec{n} the unitary inside normal vector to the SPP, v_{spp} the velocity imposed to the SPP interfaces (Equation (5)) and \vec{v} the resulting velocity field imposed through a convection equation to φ_{spp} (see [13]).

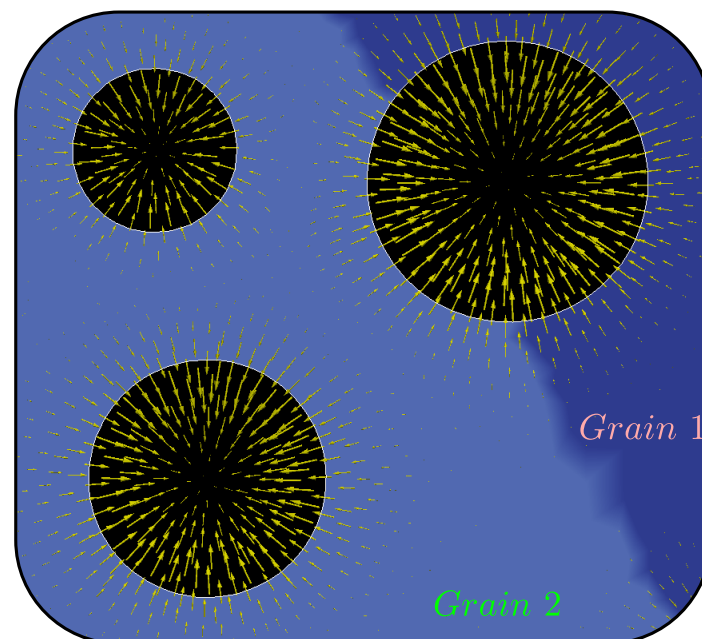


Figure 10. Smoothed precipitate interface velocity (\vec{v}) for three circular precipitates (black circles).

5. Full-Field Simulation for the Identification of GB Parameters and GG

Before developing the GG simulations, the parameters describing the GB migration of the considered material must be identified for each alloy to provide the best agreement between the numerical results and the experimental data.

5.1. AD730 Superalloy

5.1.1. Parameter Identification and Validation

Section 3.6 describes the procedure used to calculate M_0 and Q_m , the steps are more detailed below.

Supersolvus heat treatments were performed between 1120 °C and 1160 °C for several holding times (see Figure 9a). A first approximation of $M\gamma_{BT}$ was obtained through Equation (7) and then used to run the full-field simulations, where a large number of grains needs to be considered in order to be as representative as possible. Consequently, a highly performant Lagrangian model called ToRealMotion (TRM) [74] was preferred to the LS methodology in this identification part to improve the “Number of grains/calculation time” ratio. In the case of the AD730 alloy, 180,000 initial grains were simulated, with an arithmetic mean diameter $\bar{D} = 9.2 \mu\text{m}$ and a domain size of 4.3 mm \times 4.3 mm. Then, a L^2 error minimization was made between the numerical results and experimental solvus data to obtain the fitted $M\gamma$ value. Finally, the Q_m and M_0 parameters were refined using the new $M\gamma$ values and the Arrhenius law, leading to $M_0 = 2.9 \cdot 10^{25} \text{ m}^4/\text{J} \cdot \text{s}$, $Q_m = 9.8 \cdot 10^5 \text{ J/mol}$.

Supersolvus GG simulations were again performed with the identified GB mobility parameters, then compared with the experimental data of the AD730 material. Figure 11 presents the results of supersolvus GG simulations at supersolvus temperatures for the AD730 material.

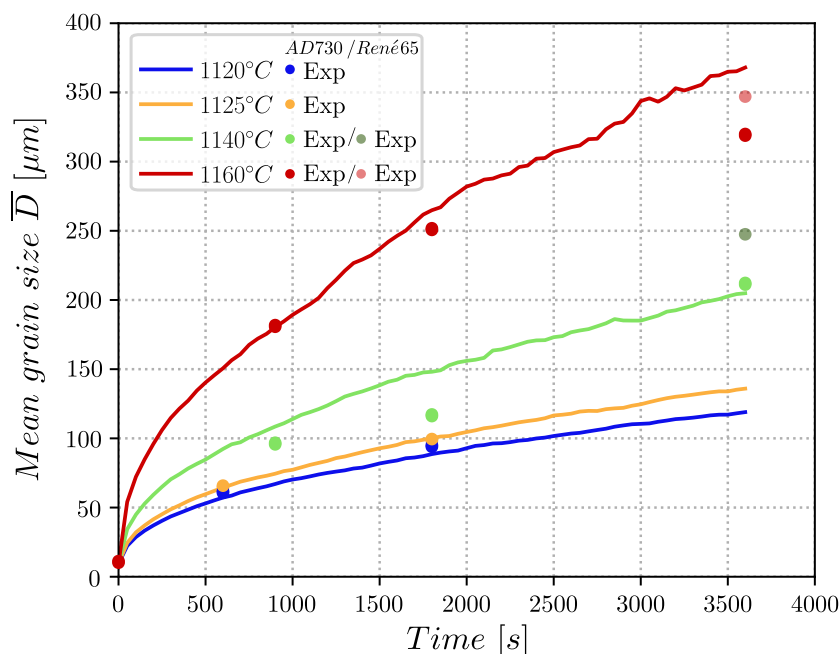


Figure 11. GG experimental data and simulations for different supersolvus heat treatments, to calibrate and validate the GB migration parameters M_0 and Q_m values for the AD730/René 65 superalloys.

The results are in good agreement with the experimental points. We can conclude, therefore, that the approach used to identify the properties gave a good approximation of M_0 and Q_m values at the supersolvus domain, and they will be used in the subsolvus simulations.

The René 65 alloy has similar behavior compared to the AD730 alloy concerning the γ' area fraction evolution, due to the similarity of their chemical compositions and their respective T_{solvus} . It will also be considered that their properties, such as the GB energy (γ), the pre-exponential factor (M_0) and the activation energy (Q_m), are similar for both materials. Given such similarity, the full-field simulations were performed only for the AD730 material, assuming that the simulation results will be very close for the René 65 superalloy

(as confirmed in Figure 11). Once the material parameters have been validated, we can proceed with the *full-field* GG simulations taking into account the identified parameters in this section and the γ' phase dissolution described in Section 3.2.

5.1.2. GG with Primary γ' Precipitate Dissolution

A pre-simulation was made in order to generate an initial numerical microstructure similar to the one observed experimentally (where the SPP are mainly located at the GB); thus, a short heat treatment of $400\text{ s} \approx 6\text{ min}$ at $1070\text{ }^\circ\text{C}$ was simulated starting from an initial smaller mean grain size than the one measured in order to get the boundaries stopping at the SPP.

The resulting initial state (after 400 s) consists of about 13,000 grains generated with an LS Laguerre–Voronoi tessellation [75]. The arithmetic mean grain radius is equal to $\bar{D} = 9.4\text{ }\mu\text{m}$, and an initial polydisperse and spherical precipitate population was generated by using the experimental γ' precipitate size distribution with an initial area fraction $f_{spp} = 12.5\%$ and a mean size $\bar{D}_{spp} = 2.1\text{ }\mu\text{m}$ (about 27,000 SPP were generated); all SPP are considered to be incoherent.

The size of the domain is $1\text{ mm} \times 1\text{ mm}$, and a time step of 5 s was considered to describe the precipitate/GB interaction correctly. The simulation parameters are $M_0 = 2.9 \cdot 10^{25}\text{ m}^4/\text{J} \cdot \text{s}$, $Q_m = 9.8 \cdot 10^5\text{ J/mol}$ as calculated in Section 5.1.1, $\gamma = 0.6\text{ J/m}^2$ [53], and $T_{solvus} = 1108\text{ }^\circ\text{C}$, as determined in Section 3.1.

Different isothermal heat treatments of 4 h were considered from $T = 1060\text{ }^\circ\text{C}$ (i.e., $T_{solvus} - 50\text{ }^\circ\text{C}$) up to the solvus temperature. The precipitate interface velocity v_{spp} is calculated using Equation (5).

The evolution of the primary γ' precipitate area fraction for the AD730 alloy is given by Equations (1) and (4). Figure 12 presents the results obtained from the LS simulations. Regarding the precipitate area fraction evolution (Figure 12a), the full-field simulations reproduce, as expected, the phenomenological model. Most importantly, these results agree with the experimental grain size evolution, even if the mobility was extrapolated from the supersolvus domain to the subsolvus domain.

Figure 12b illustrates the mean precipitate size evolution, for the numerical treatment at $1060\text{ }^\circ\text{C}$, where the primary γ' phase fraction does not change, neither does the size of the precipitates; for temperatures between $1070\text{ }^\circ\text{C}$ and $1090\text{ }^\circ\text{C}$, the size of the precipitate decreases during the first minutes due to the dissolution mechanism, but then the average size increases as the smallest precipitates disappear and eventually reaches a stable value. Finally, for the temperatures $1100\text{ }^\circ\text{C}$ and $1110\text{ }^\circ\text{C}$, the dissolution is more significant and the mean size of the precipitates decreases until the γ' phase fraction stops evolving, but for $T_{solvus} = 1108\text{ }^\circ\text{C}$, the precipitates were mostly dissolved after 1 h of annealing. As discussed in the experimental Section 3.3, the Ostwald ripening mechanism is likely to occur after 1 h when the γ' phase fraction remains constant. However, this phenomenon is not taken into account in the *mean-field model* used to describe the evolution of the precipitates and thus also not in the *full-field* simulations. The evolution of the numbers of precipitates and grains along the simulation is shown in Figure 12c,d, respectively.

Finally, Figure 12e illustrates the arithmetic mean grain size evolution for all tests. When the heat treatment is far from the T_{solvus} (i.e., $1060\text{ }^\circ\text{C}$, $1070\text{ }^\circ\text{C}$), the SPP completely blocks the grains boundaries. However, for temperatures between $1080\text{--}1100\text{ }^\circ\text{C}$ where the precipitates dissolve, the grains can grow until they find their new equilibrium state, which is reached when precipitate dissolution ends (if the Ostwald ripening mechanism was taken into account, the grains would be expected to keep evolving slowly, as the increase of mean precipitate radius at constant fraction reduces the pinning pressure and releases the GB). For the HT at the solvus temperature ($1110\text{ }^\circ\text{C}$), the precipitates dissolve rapidly and the grains can grow freely when no precipitate remains. These tests show that the used numerical framework can consider the evolution of SPP and predict the grain size not only at long annealing times when the SPP have reached their equilibrium fraction but also in the transient regime. These results validate the possibility of reproducing the precipitate

dissolution with a phenomenological model used in LS full-field simulations to predict the material behavior with a good compromise between accuracy and simplicity.

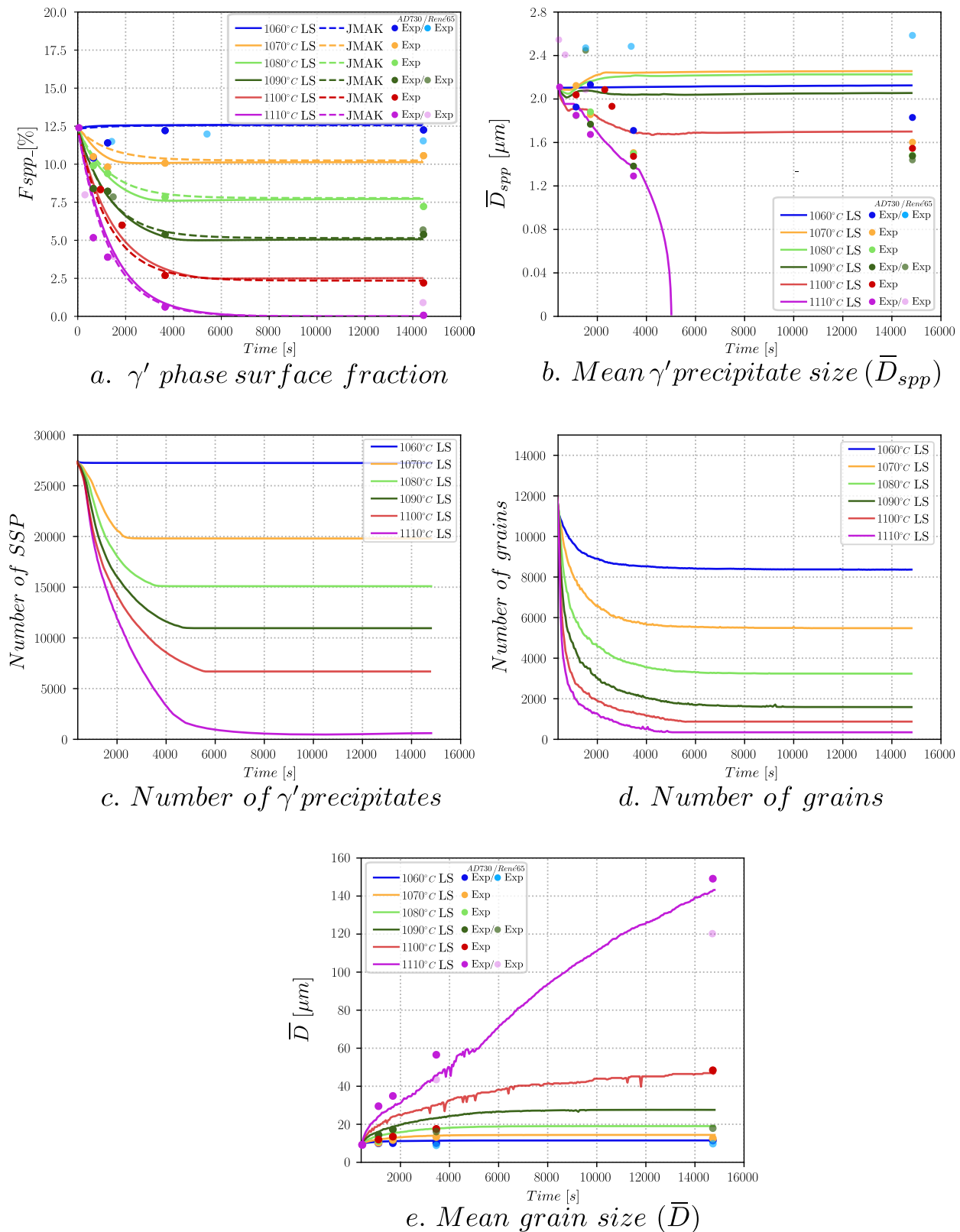


Figure 12. Simulation results for the AD730 superalloy for different temperatures from T_{solvus} to 50° below it.

5.2. N19 Superalloy

5.2.1. Parameter Identification and Validation

Since the N19 is a PM superalloy, the identification procedure was slightly different. This type of alloy has indeed a specific GG evolution. At supersolvus temperatures, the mean grain size evolves up to a maximum size (about 20 μm) and then remains constant. Thus, the identification process was only carried out during the first 20 min of heat treatments, where GG was observed to occur. The supersolvus treatments were made at 1160 $^{\circ}\text{C}$ and 1180 $^{\circ}\text{C}$, once the first approximation of $M\gamma_{BT}$ was obtained through Equation (7). The first sets of TRM simulations were run with the precalculated parameters, and 40,000 initial grains were considered, with arithmetic mean diameter $\bar{D} = 3 \mu\text{m}$ and a domain size of 0.5 mm \times 0.5 mm. Then, a L^2 error minimization was made using the numerical results and the experimental supersolvus data to obtain a fitted $M\gamma$ value. Finally, the Arrhenius law was used to calculate the parameter values of the N19 material, which are $M_0 = 0.51 \text{ m}^4/\text{J} \cdot \text{s}$ and $Q_m = 3.3 \cdot 10^5 \text{ J/mol}$.

Figure 13 presents the experimental data and the supersolvus simulations (dashed lines) obtained with the identified properties. These simulations only match the experimental points at the HT onset. These results show a lack in the material description that we need to consider to reproduce and predict the real microstructure evolution.

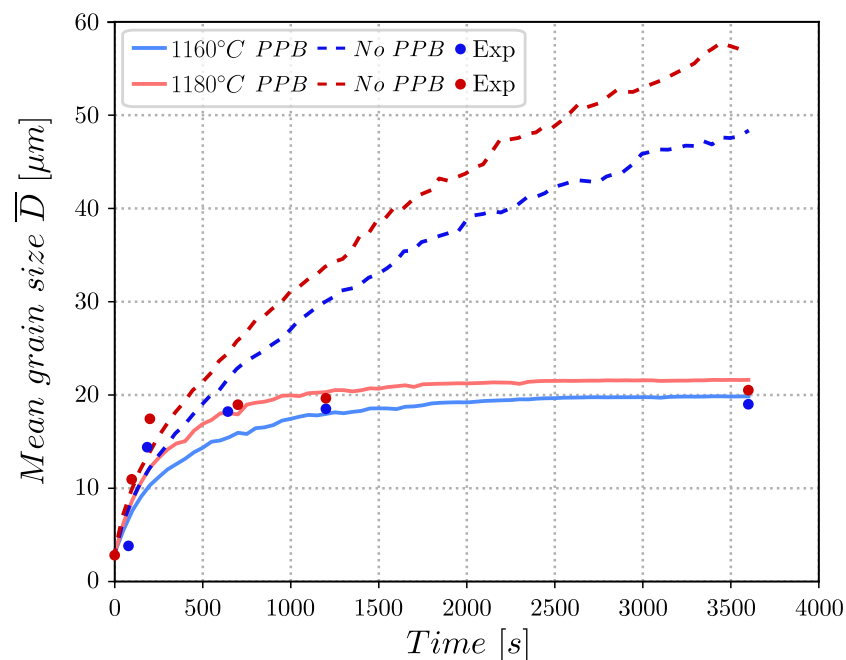


Figure 13. GG simulations at supersolvus temperatures to calibrate and validate the identified the GB migration parameters M_0 and Q_m values for the N19 superalloy.

The reason for the grain size stagnation is likely to be that Prior Particle Boundary (PPB) particles block the grains boundaries as often observed in PM materials. Then, to correctly predict GG, it is necessary to consider this additional type of particle population in the simulations.

- *Simulation of Prior Particles Boundary (PPB) particles*

Such kind of additional precipitate population is common in PM materials, and they have been largely studied experimentally [76–78]. The PPB form at the surface of the initial powder grains, and they usually consist of oxides, carbides, or oxy-carbides. It is commonly accepted that PPB particles result from segregations or surface contamination. A slight dissolution [79] and coarsening [80,81] of these precipitates have been observed in materials submitted to high temperatures.

Some numerical works have been developed to account for their presence, for instance, using a particle packing in [82] and an FE framework in [83].

Here, the PPB particles will be treated as a population of oxides that will not evolve; thus, they will be considered as static particles located in the interfaces of the initial powder grains. Therefore, to generate the PPB network, a Laguerre–Voronoi tessellation was used considering the experimental size distribution of the initial powders (mean $D_{\text{powder}} = 25 \mu\text{m}$), followed by the generation of the PPB particles at the boundaries of the tessellation (see Figure 14). The PPB particles are considered as a new distance function in our LS approach. Once the PPB particles were generated, the actual initial polycrystal was statistically generated (several grains/crystals per powder grain), and, finally, the GG simulation was performed.

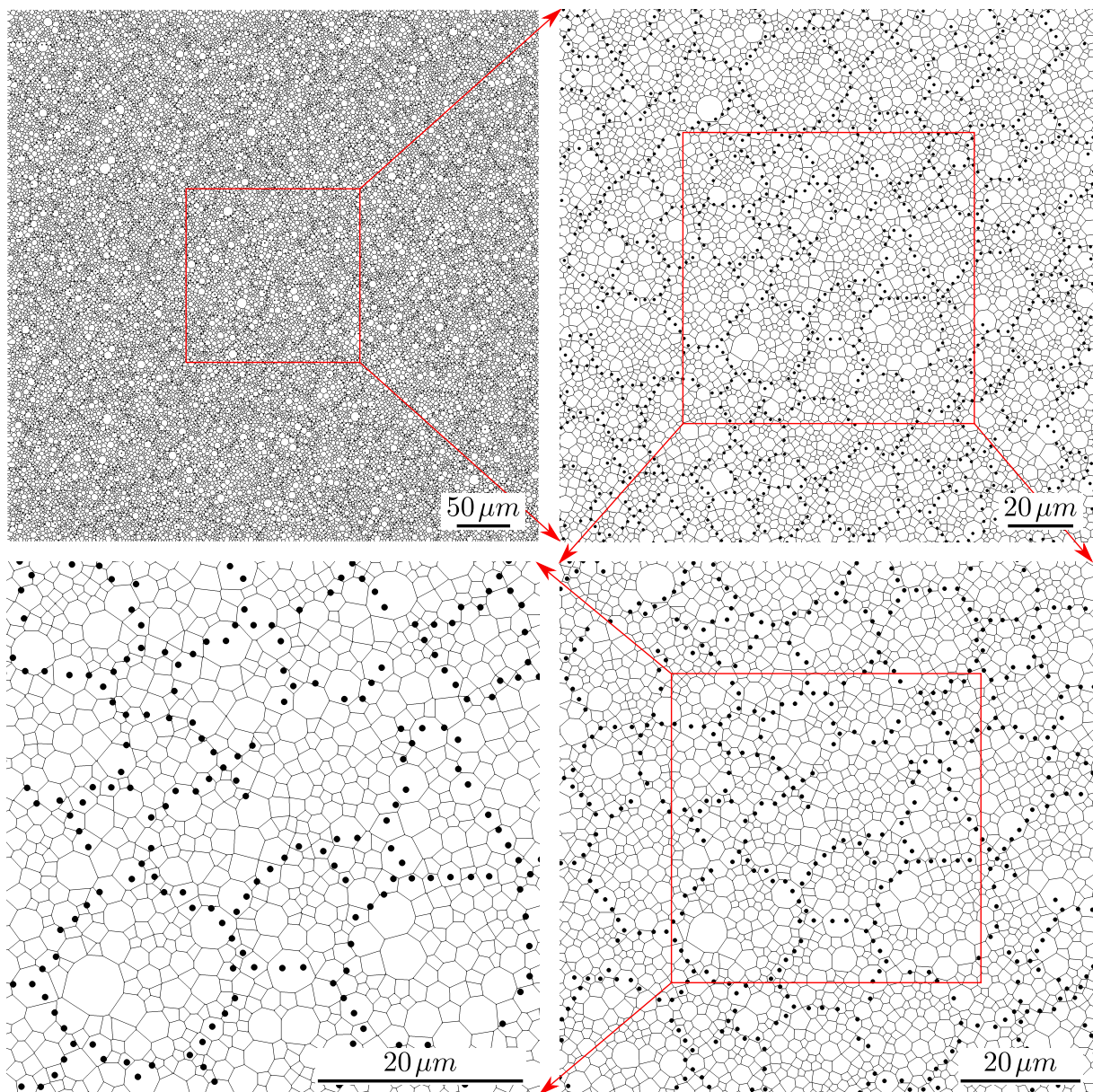


Figure 14. Successive zooms illustrating the initial statistical microstructure used to describe the N19 superalloy with the black PPB particles.

The validation of the identified properties for the *N19* material was made once again with the new considered topology with $f_{PPB} = 2\%$ and a homogeneous precipitate size $D_{PPB} = 1 \mu\text{m}$. Although these values are large concerning the actual characteristics of the PPB [79,80], they enable, in Smith–Zener meaning (i.e., by respecting the ratio f_{PPB}/D_{PPB} while increasing by around a factor 10 the respective values of D_{PPB} and f_{PPB}), to respect a representative pinning pressure resulting from this PPB particles population. Indeed, in terms of numerical cost of the meshing adaptation and subsequent simulations, it will not be realistic to consider a large number of nanoparticles.

The results are presented in Figure 13 (solid lines). The mean grain size prediction is in very good agreement with the experimental data, where the PPB particles block the grain boundaries. The predicted final mean grain size (about $20 \mu\text{m}$) corresponds approximately to the mean size of the initial powders as a result of the strong pinning pressure exerted by the small PPB particles.

Once the material parameter values have been established, the full-field GG simulations can be performed, taking into account the identified GB migration parameters, the γ' precipitate dissolution described in Section 3.2, and by considering or not PPB particles.

5.2.2. GG with Primary γ' Precipitate Dissolution

A pre-simulation was also made as for the *AD730*, but for a HT of 100 s at $1110 \text{ }^\circ\text{C}$. The initial state (after 100 s) consists of around 33,000 grains generated with an LS Laguerre–Voronoi tessellation [75]. The arithmetic mean grain diameter $\bar{D} = 3 \mu\text{m}$ and an initial spherical primary γ' precipitate population with a area fraction $f_{spp} = 18.5\%$ and a mean size $\bar{D}_{spp} = 1.3 \mu\text{m}$ (about 32,000 incoherent SPP) are considered.

The size of the domain is $0.5 \text{ mm} \times 0.5 \text{ mm}$ (see Figure 15 but without the red particles), and the considered time step was 5 s. The simulation parameters were $M_0 = 0.51 \text{ m}^4/\text{J} \cdot \text{s}$, $Q_m = 3.3 \cdot 10^5 \text{ J/mol}$ as calculated in Section 5.2.1, $\gamma = 0.6 \text{ J/m}^2$ [53] and $T_{solvus} = 1150 \text{ }^\circ\text{C}$ as determined in Section 2.1.1.

Simulations considering or not the PPB particles, in addition to the evolving γ' precipitates, were carried out to understand how they affect the GG behavior.

- Simulations without considering the PPB particles

Different isothermal heat treatments (4 h) around T_{solvus} were simulated. The primary γ' precipitate interface velocity was calculated according to Equation (5).

The primary γ' phase area fraction evolution for the *N19* was obtained by Equations (2) and (4).

Figure 16a shows that the γ' phase area fraction evolution matches the phenomenological model and the experimental data. The mean primary γ' precipitate size evolution is presented in Figure 16b where there is a slight decrease at the beginning of the simulation; then, as the small precipitates continue to dissolve, the mean grain size tends to increase. Figure 16c,d illustrate the number evolution of the γ' precipitates and grains, respectively. The GB kinetics is so fast that it makes the smallest grains disappear during the first minutes of the simulations.

Finally, Figure 16e shows the arithmetic mean grain size evolution for all the simulations. As discussed before, the mean grain size evolves during the γ' precipitate dissolution. However, the grain size reaches a stable value once the dissolution stops. As expected for this case, a grain size larger than the one observed experimentally is reached. Indeed, for the HT at $1150 \text{ }^\circ\text{C}$, the predicted grain size continues to increase contrary to the experimental points that stagnate at about $20 \mu\text{m}$.

- Simulations considering the PPB particles

The PPB particles were generated at the Laguerre–Voronoi tessellation boundaries based on the experimental granulometry of the initial powder of this material (see Section 3.2). The initial state is the same used previously for the N19 (see Figure 15). However, for this case, an additional static particle population was introduced ($f_{PPB} = 2\%$ of size $\bar{D}_{PPB} = 1 \mu\text{m}$, red particles).

Figure 17 illustrates the microstructure evolution for some HT at different times and temperatures along the simulation and the results are summarized in Figure 18.

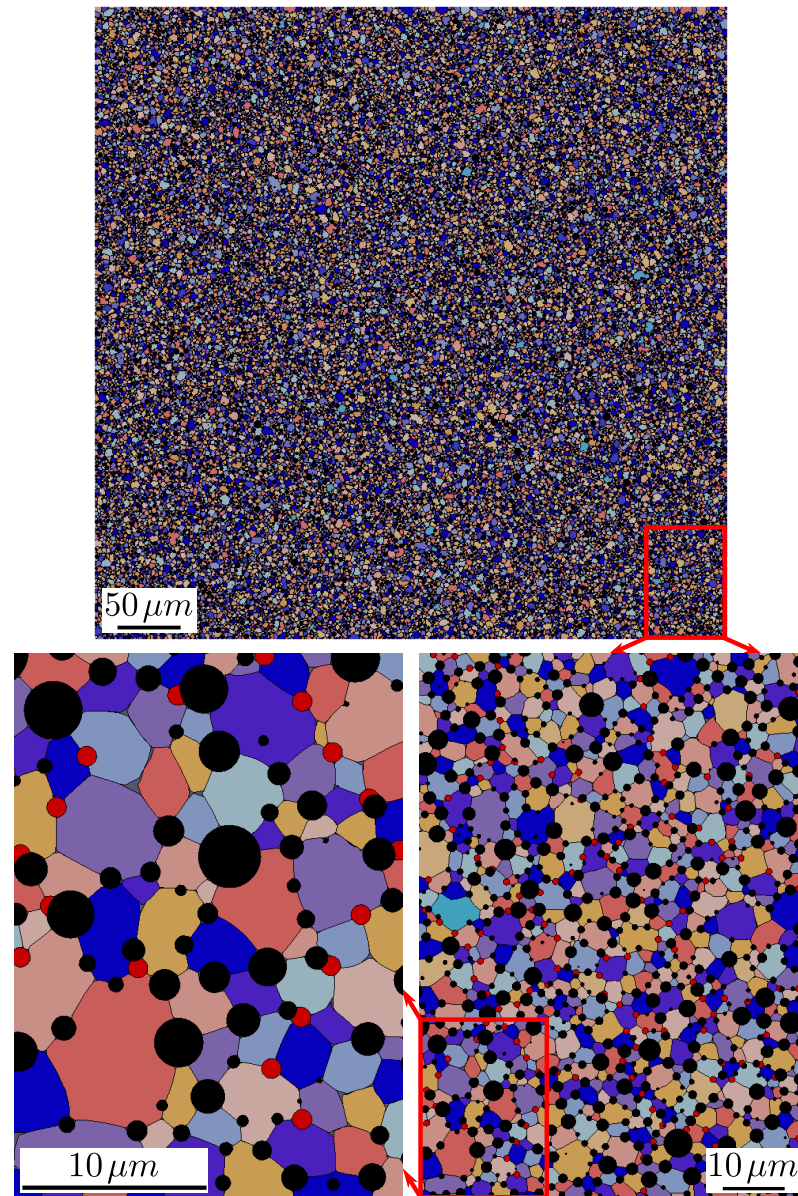
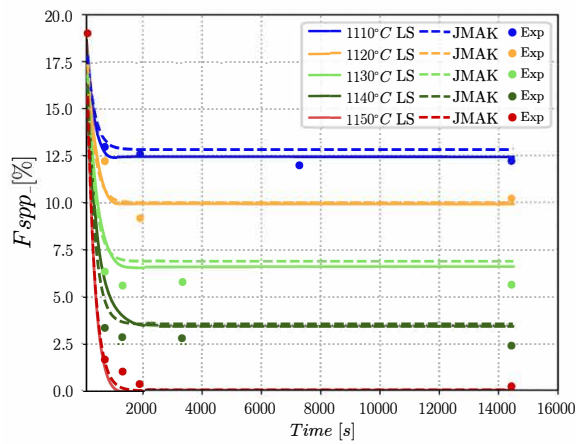
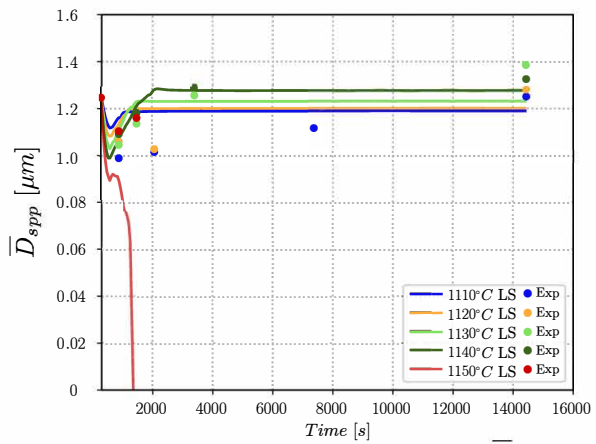


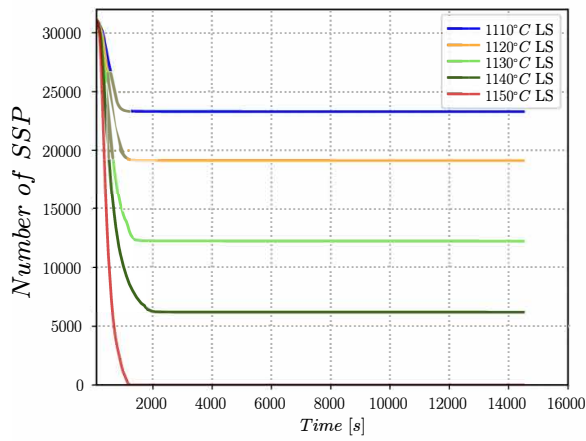
Figure 15. Initial state of the microstructure used in the simulations for the N19 material with γ' precipitates (black) and PPB particles (red).



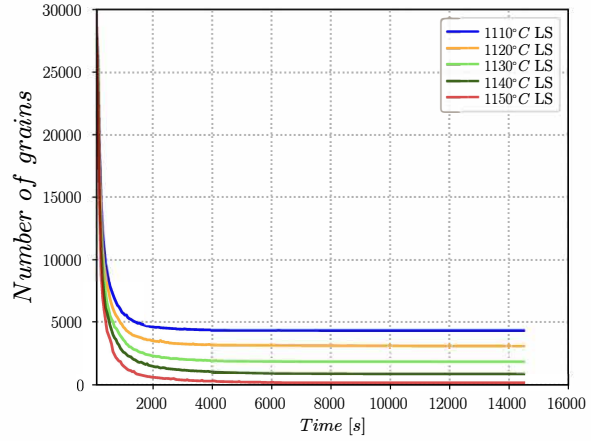
a. γ' phase surface fraction



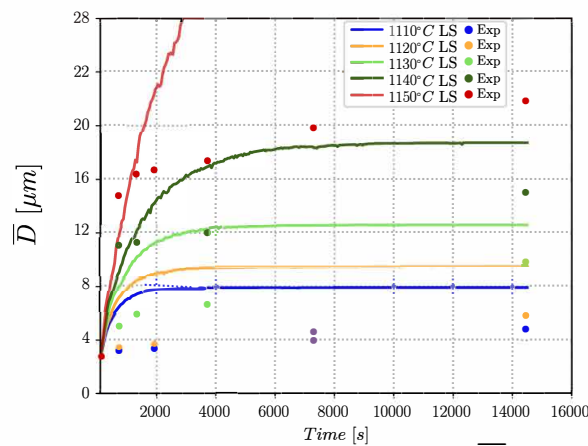
b. Mean γ' precipitate size (\bar{D}_{spp})



c. Number of γ' precipitates



d. Number of grains



e. Mean grain size (\bar{D})

Figure 16. Simulation results for the N19 superalloy without considering the PPB particles.

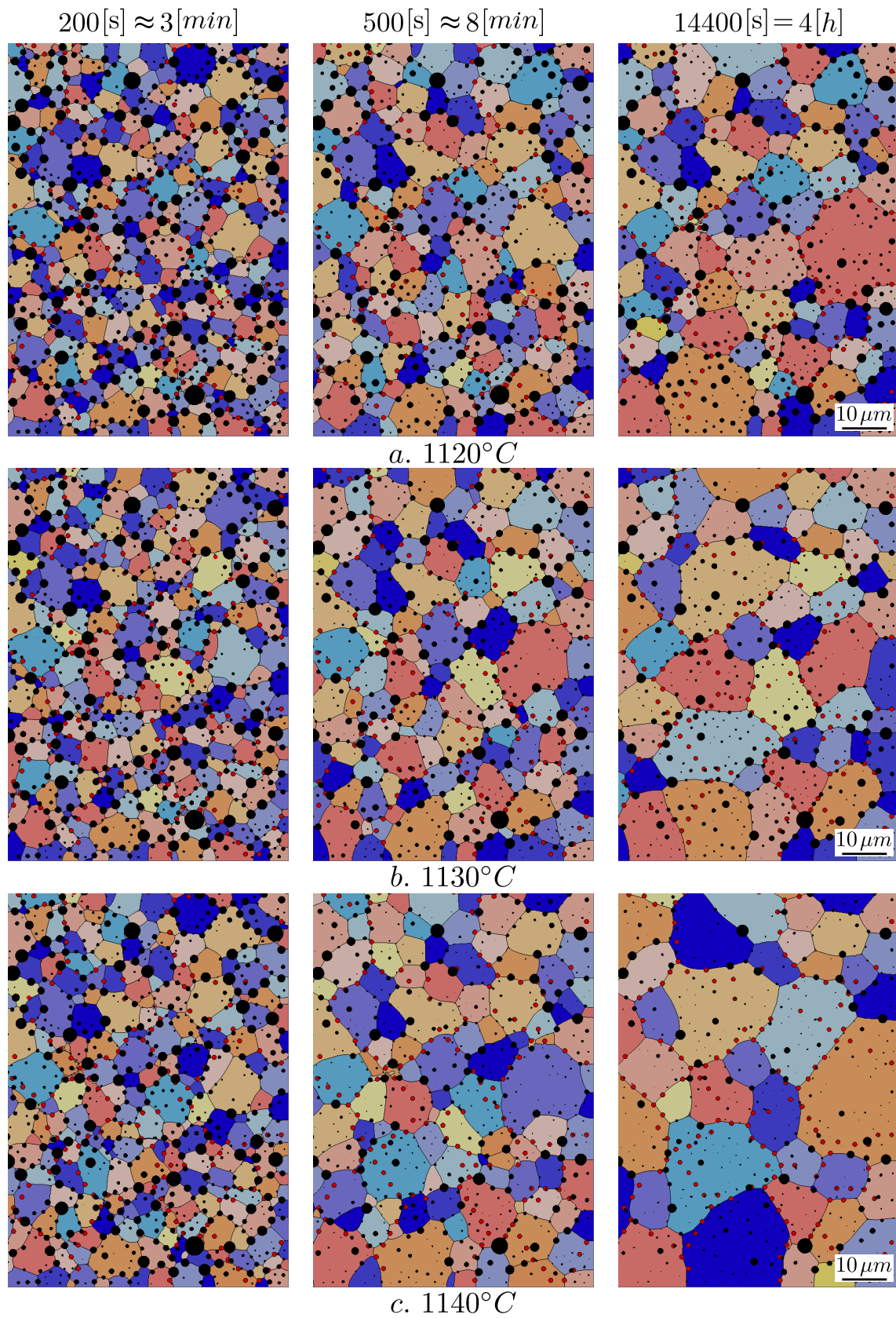


Figure 17. GG simulations for the N19 material with both evolving primary γ' precipitates (black) and static PPB particles (red) at subsolvus temperatures for different heat treatment and times (200 s, 500 s, and 14,400 s) for a zoomed area of the 0.5 mm \times 0.5 mm simulation domain.

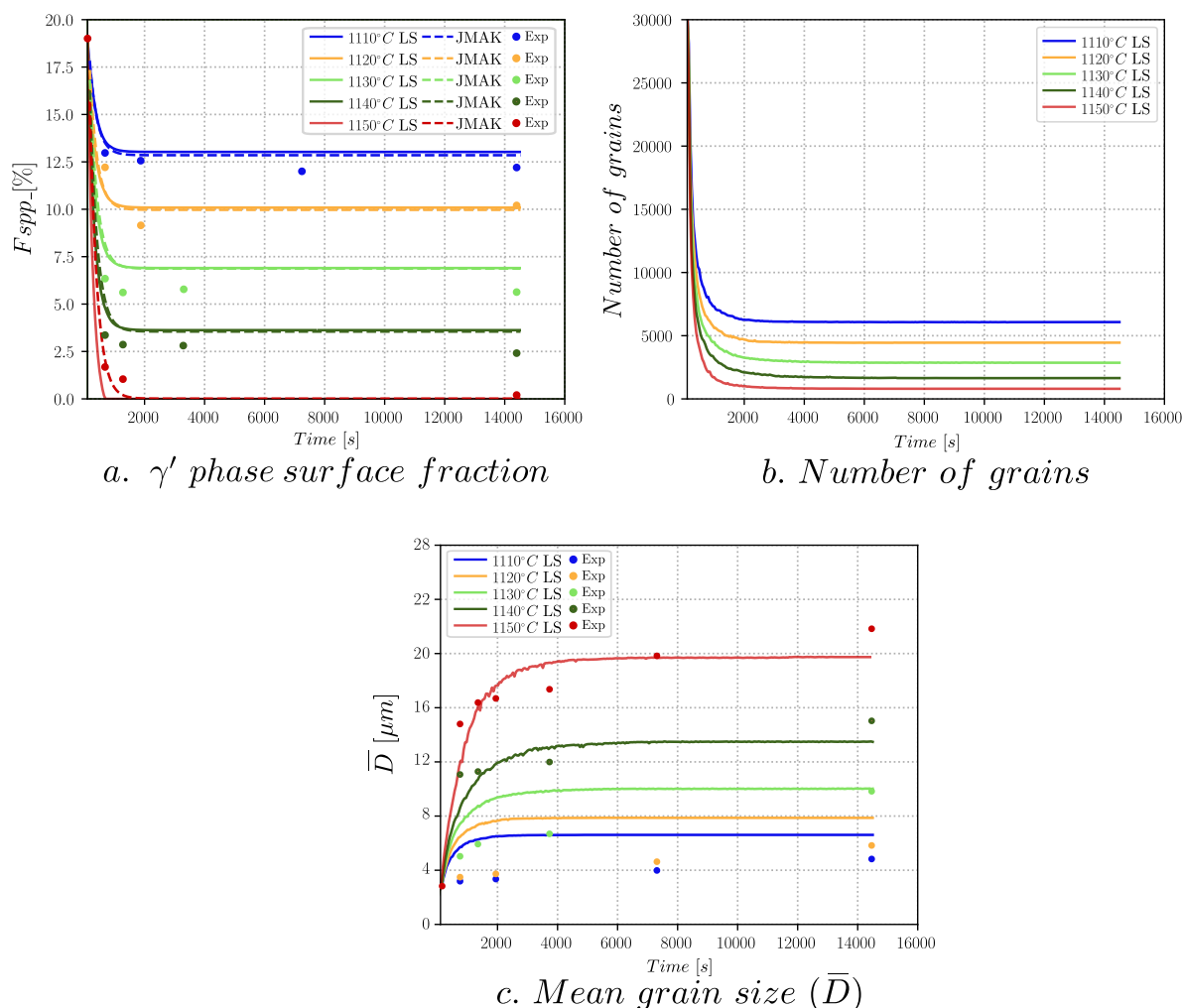


Figure 18. Simulation results for the N19 superalloy taking into account both the evolving primary γ' phase and the static PPB particles.

The γ' area fraction evolution (Figure 18a) is similar to one of (Figure 16a) because the primary γ' interface velocity is the same. Considering the static PPB particles, the predicted arithmetic mean grain size is in better agreement with the experimental data as illustrated in Figure 18c. The LS simulations describe very well the limiting grain size independently of the temperature.

Figure 19 illustrates the microstructural evolution for both the considered cases (with or without PPB particles) at 1150 °C, and allows us to visualize how the grains continue to grow when no γ' precipitate remains and PPB particles are not taken into account. On the contrary, when static PPB particles are simulated, the grains' boundaries are blocked by their network, limiting the mean grain size slightly below the initial powder size of the material.

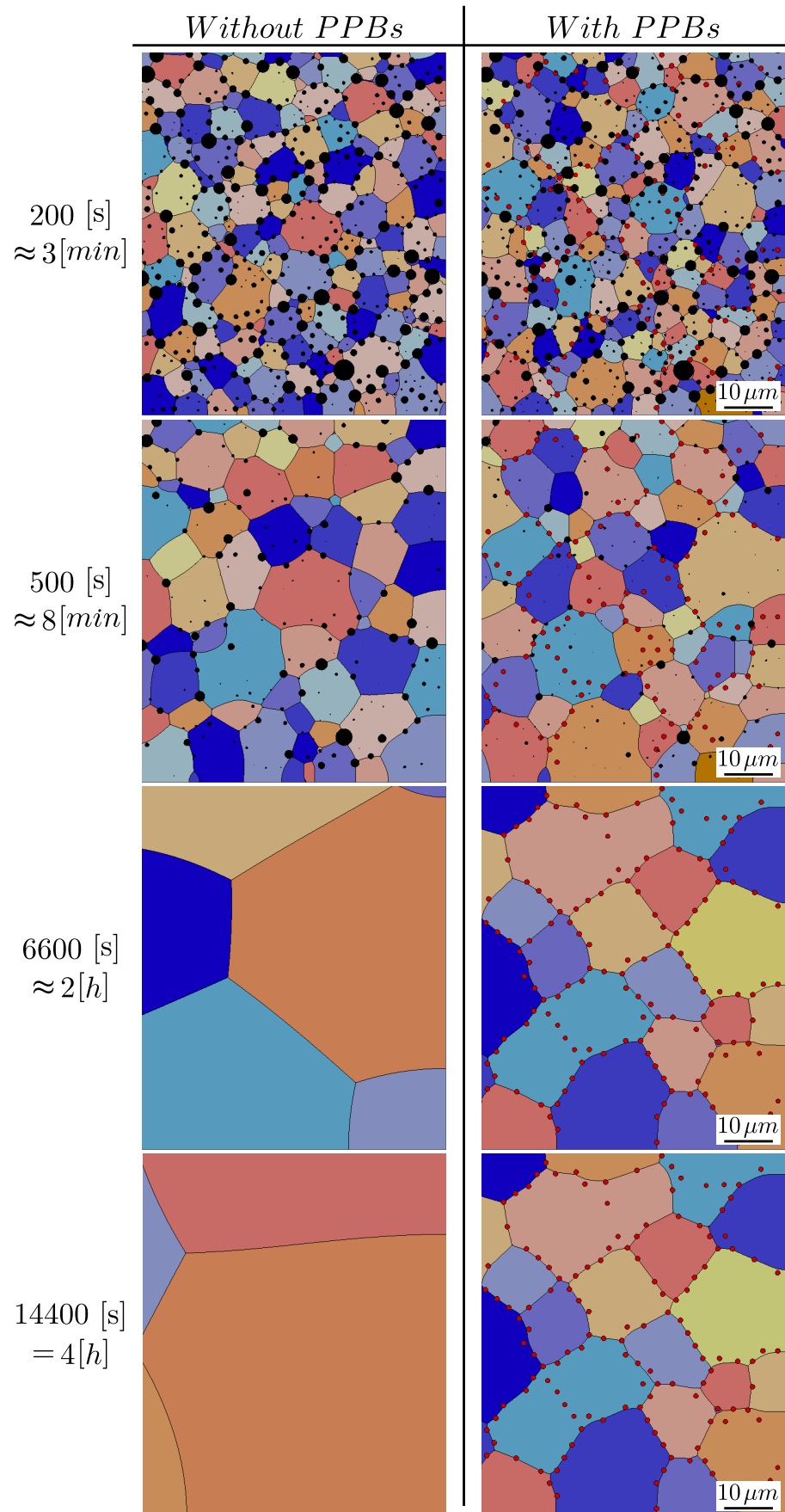


Figure 19. Comparison of the simulated microstructure evolution of the N19 superalloy considering or not the PPB particles (red) at 1150 °C for a zoomed area of the 0.5 mm × 0.5 mm simulation domain.

6. Conclusions

A new approach using a mean-field model to describe the dissolution of second phase particles was introduced in a finite element framework using the Level-Set model to simulate grain growth for different γ - γ' nickel base superalloys as primary γ' precipitates dissolve.

The dissolution kinetics of primary γ' precipitates was studied in the AD730, René 65 and N19 alloys. *Thermo-Calc* curves and a JMAK approximation were used to establish an equation for describing the primary γ' phase fraction evolution as a function of temperature and time, which is valid from T_{solvus} to 50 °C below for each alloy ($T_{solvus} - 50 \leq T \leq T_{solvus}$). It was shown that the particle evolution for the two conventional cast and wrought alloys (AD730, René 65) was very similar. Therefore, the same equation was used to reproduce the primary γ' dissolution in both alloys. For the powder metallurgy alloy (N19), the dissolution kinetics was faster.

The LS simulation results respect the imposed phenomenological equation and so there is a good agreement with the experimental data concerning the second phase precipitate evolution. These results confirm the possibility of considering a simple phenomenological model to describe the precipitate evolution to get good accuracy in terms of the predicted precipitate and grain sizes, including both the transient regime at short times and the steady-state at longer annealing times.

Moreover, the possibility of considering the Prior Particles Boundaries (PPB) particles has been introduced in the simulations of the powder metallurgy N19 alloy. The numerical results are consistent with the observations, where these PPB particles limit the mean grain size to about the mean size of the initial alloy powder.

The current perspectives of this work concern the use, in 2D and 3D, of the proposed methodology to discuss other mechanisms, such as the Ostwald ripening and precipitation.

Author Contributions: Conceptualization, K.A., M.B., N.B.; software, K.A., S.F., B.F., M.B.; validation, K.A.; formal analysis, K.A., I.J.; investigation, K.A., I.J.; resources, J.-M.F., D.L., C.D.; project administration, M.B., N.B.; funding acquisition, M.B., N.B.; writing—original draft preparation, K.A., I.J., M.B.; writing—review and editing, K.A., I.J., N.B., M.B., D.L.; supervision, N.B., M.B. All authors have read and agreed to the published version of the manuscript.

Funding: This research was funded by ArcelorMittal, ASCOMETAL, AUBERT & DUVAL, CEA, FRAMATOME, TIMET, Constellium and TRANSVALOR companies and the ANR through the DIGIMU and TOPAZE consortium and ANR industrial Chairs (Grant No. ANR-16-CHIN-0001 and ANR-19-CHIN-0005).

Institutional Review Board Statement: Not applicable.

Informed Consent Statement: Not applicable.

Data Availability Statement: The experimental data necessary to reproduce these findings are available from the corresponding author on request.

Acknowledgments: The authors thank Jérôme Blaizot and Chi-Toan Nguyen for the fruitful discussions that made possible this study.

Conflicts of Interest: The authors declare no conflict of interest.

References

1. Giraud, R.; Hervier, Z.; Cormier, J.; Saint-Martin, G.; Hamon, F.; Milhet, X.; Mendez, J. Strain effect on the γ' dissolution at high temperatures of a nickel-based single crystal superalloy. *Metall. Mater. Trans. A* **2013**, *44*, 131–146. [[CrossRef](#)]
2. Grosdidier, T.; Hazotte, A.; Simon, A. Precipitation and dissolution processes in γ/γ' single crystal nickel-based superalloys. *Mater. Sci. Eng. A* **1998**, *256*, 183–196. [[CrossRef](#)]
3. Fan, X.; Guo, Z.; Wang, X.; Yang, J.; Zou, J. Morphology evolution of γ' precipitates in a powder metallurgy Ni-base superalloy. *Mater. Charact.* **2018**, *139*, 382–389. [[CrossRef](#)]
4. Smith, C. Introduction to grains, phases, and interfaces—an interpretation of microstructure. *Trans. AIME* **1948**, *175*, 15–51.
5. Zener, C. Theory of growth of spherical precipitates from solid solution. *J. Appl. Phys.* **1949**, *20*, 950–953. [[CrossRef](#)]
6. Manohar, P.A.; Ferry, M.; Chandra, T. Five decades of the Zener equation. *ISIJ Int.* **1998**, *38*, 913–924. [[CrossRef](#)]

7. Rios, P.R. Overview no. 62: A theory for grain boundary pinning by particles. *Acta Metall.* **1987**, *35*, 2805–2814. [[CrossRef](#)]
8. Soucail, M.; Bienvenu, Y. Dissolution of the γ' phase in a nickel base superalloy at equilibrium and under rapid heating. *Mater. Sci. Eng. A* **1996**, *220*, 215–222. [[CrossRef](#)]
9. Masoumi, F.; Jahazi, M.; Cormier, J.; Shahriari, D. Dissolution kinetics and morphological changes of γ' in AD730™. *MATEC Web Conf.* **2014**, *14*, 13005. [[CrossRef](#)]
10. Semiatin, S.L.; Levkulich, N.C.; Saurber, A.E.; Mahaffey, D.W.; Payton, E.J.; Senkov, O.N. The kinetics of precipitate dissolution in a nickel-base superalloy. *Metall. Mater. Trans. A* **2017**, *48*, 5567–5578. [[CrossRef](#)]
11. Masoumi, F.; Jahazi, M.; Shahriari, D.; Cormier, J. Coarsening and dissolution of γ' precipitates during solution treatment of AD730™ Ni-based superalloy: Mechanisms and kinetics models. *J. Alloys Compd.* **2016**, *658*, 981–995. [[CrossRef](#)]
12. Huang, H.; Liu, G.; Wang, H.; Ullah, A.; Hu, B. Dissolution behavior and kinetics of γ' phase during solution treatment in powder metallurgy Nickel-based superalloy. *Metall. Mater. Trans. A* **2020**, *51*, 1075–1084. [[CrossRef](#)]
13. Alvarado, K.; Florez, S.; Flipon, B.; Bozzolo, N.; Bernacki, M. A level set approach to simulate grain growth with an evolving population of second phase particles. *Model. Simul. Mater. Sci. Eng.* **2021**, *29*, 035009. [[CrossRef](#)]
14. Xuan, C.; Mu, W. Dissolution kinetics of arbitrarily-shaped alumina in oxide melt: An integration of phase-field modelling and real-time observation study. *J. Alloys Compd.* **2020**, *834*, 155168. [[CrossRef](#)]
15. Wang, G.; Xu, D.S.; Ma, N.; Zhou, N.; Payton, E.J.; Yang, R.; Mills, M.J.; Wang, Y. Simulation study of effects of initial particle size distribution on dissolution. *Acta Mater.* **2009**, *57*, 316–325. [[CrossRef](#)]
16. Miodownik, M.; Holm, E.A.; Hassold, G.N. Highly parallel computer simulations of particle pinning: Zener vindicated. *Scr. Mater.* **2000**, *42*, 1173–1177. [[CrossRef](#)]
17. Anderson, M.P.; Grest, G.S.; Doherty, R.D.; Li, K.; Srolovitz, D.J. Inhibition of grain growth by second phase particles: Three dimensional Monte Carlo computer simulations. *Scr. Metall.* **1989**, *23*, 753–758. [[CrossRef](#)]
18. Gao, J.; Thompson, R.G.; Patterson, B.R. Computer simulation of grain growth with second phase particle pinning. *Acta Mater.* **1997**, *45*, 3653–3658. [[CrossRef](#)]
19. Srolovitz, D.J.; Anderson, M.P.; Grest, G.S.; Sahni, P.S. Computer simulation of grain growth-III. Influence of a particle dispersion. *Acta Metall.* **1984**, *32*, 1429–1438. [[CrossRef](#)]
20. Raabe, D. Introduction of a scalable three-dimensional cellular automaton with a probabilistic switching rule for the discrete mesoscale simulation of recrystallization phenomena. *Philos. Mag. A* **1999**, *79*, 2339–2358. [[CrossRef](#)]
21. Raabe, D.; Hantcherli, L. 2D cellular automaton simulation of the recrystallization texture of an IF sheet steel under consideration of Zener pinning. *Comput. Mater. Sci.* **2005**, *34*, 299–313. [[CrossRef](#)]
22. Weygand, D.; Bréchet, Y.; Lépinoux, J. Zener pinning and grain growth: A two-dimensional vertex computer simulation. *Acta Mater.* **1999**, *47*, 961–970. [[CrossRef](#)]
23. Moelans, N.; Blanpain, B.; Wollants, P. Phase field simulations of grain growth in two-dimensional systems containing finely dispersed second-phase particles. *Acta Mater.* **2006**, *54*, 1175–1184. [[CrossRef](#)]
24. Moelans, N.; Blanpain, B.; Wollants, P. Pinning effect of second-phase particles on grain growth in polycrystalline films studied by 3D phase field simulations. *Acta Mater.* **2007**, *55*, 2173–2182. [[CrossRef](#)]
25. Chang, K.; Feng, W.; Chen, L.Q. Effect of second-phase particle morphology on grain growth kinetics. *Acta Mater.* **2009**, *57*, 5229–5236. [[CrossRef](#)]
26. Apel, M.; Böttger, B.; Rudnizki, J.; Schaffnit, P.; Steinbach, I. Grain growth simulations including particle pinning using the multiphase-field concept. *ISIJ Int.* **2009**, *49*, 1024–1029. [[CrossRef](#)]
27. Darvishi Kamachali, R.; Steinbach, I. 3D phase-field simulation of grain growth: Topological analysis versus mean-field approximations. *Acta Mater.* **2012**, *60*, 2719–2728. [[CrossRef](#)]
28. Schwarze, C.; Darvishi Kamachali, R.; Steinbach, I. Phase-field study of Zener drag and pinning of cylindrical particles in polycrystalline materials. *Acta Mater.* **2016**, *106*, 59–65. [[CrossRef](#)]
29. Chang, K.; Kwon, J.; Rhee, C.K. Effect of particle-matrix coherency on Zener pinning: A phase-field approach. *Comput. Mater. Sci.* **2018**, *142*, 297–302. [[CrossRef](#)]
30. Chakrabarti, T.; Manna, S. Zener pinning through coherent precipitate: A phase-field study. *Comput. Mater. Sci.* **2018**, *154*, 84–90. [[CrossRef](#)]
31. Agnoli, A.; Bozzolo, N.; Logé, R.; Franchet, J.M.; Laigo, J.; Bernacki, M. Development of a level set methodology to simulate grain growth in the presence of real secondary phase particles and stored energy—Application to a nickel-base superalloy. *Comput. Mater. Sci.* **2014**, *89*, 233–241. [[CrossRef](#)]
32. Scholtes, B.; Ilin, D.; Settefrati, A.; Bozzolo, N.; Agnoli, A.; Bernacki, M. Full field modeling of the Zener pinning phenomenon in a level set framework—Discussion of classical limiting mean grain size equation. In Proceedings of the International Symposium on Superalloys, Seven Springs, PA, USA, 11–15 September 2016; pp. 497–503.
33. Villaret, F.; Hary, B.; de Carlan, Y.; Baudin, T.; Logé, R.; Maire, L.; Bernacki, M. Probabilistic and deterministic full field approaches to simulate recrystallization in ODS steels. *Comput. Mater. Sci.* **2020**, *179*, 109646. [[CrossRef](#)]
34. Briesen, H. Aggregate structure evolution for size-dependent aggregation by means of Monte Carlo simulations. *KONA Powder Part. J.* **2007**, *25*, 180–189. [[CrossRef](#)]
35. Roy, I.; Balikci, E.; Ibekwe, S.; Raman, A. Precipitate growth activation energy requirements in the duplex size γ' distribution in the superalloy IN738LC. *J. Mater. Sci.* **2005**, *40*, 6207–6215. [[CrossRef](#)]

36. Chang, K.; Moelans, N. Phase-field simulations of the interaction between a grain boundary and an evolving second-phase particle. *Philos. Mag. Lett.* **2015**, *95*, 202–210. [[CrossRef](#)]
37. Heaney, J.A.; Lasonde, M.L.; Powell, A.M.; Bond, B.J.; O'Brien, C.M. Development of a new cast and wrought alloy (René 65) for high temperature disk applications. In *8th International Symposium on Superalloy 718 and Derivatives*; John Wiley & Sons: Hoboken, NJ, USA, 2014; pp. 67–77.
38. Devaux, A.; Picqué, B.; Gervais, M.F.; Georges, E.; Poulain, T.; Héritier, P. AD730™—A new Nickel-based superalloy for high temperature engine rotative parts. *Superalloys* **2012**, *2012*, 911–919.
39. Locq, D.; Nazé, L.; Franchet, J.M.; Caron, P.; Dumont, A.; Köster, A.; Guédou, J.Y. Metallurgical optimisation of PM superalloy N19. *MATEC Web Conf.* **2014**, *14*, 11007. [[CrossRef](#)]
40. Sundman, B.; Jansson, B.; Andersson, J.O. The Thermo-Calc databank system. *Calphad* **1985**, *9*, 153–190. [[CrossRef](#)]
41. Charpagne, M.A. Evolutions de microstructure au cours du forgeage de l'alliage René 65. Ph.D. Thesis, PSL Research University, Paris, France, 2016.
42. Perrut, M.; Locq, D. γ' precipitation kinetics in the powder metallurgy superalloy N19 and influence of the precipitation latent heat. *MATEC Web Conf.* **2014**, *14*, 09004. [[CrossRef](#)]
43. Abràmoff, M.D.; Magalhães, P.J.; Ram, S.J. Image processing with ImageJ. *Biophotonics Int.* **2004**, *11*, 36–42.
44. Bachmann, F.; Hielscher, R.; Schaeben, H. Texture Analysis with MTEX—Free and Open Source Software Toolbox. *Solid State Phenom.* **2010**, *160*, 63–68. [[CrossRef](#)]
45. Vernier, S.; Franchet, J.M.; Lesne, M.; Douillard, T.; Silvent, J.; Langlois, C.; Bozzolo, N. iCHORD-SI combination as an alternative to EDS-EBSD coupling for the characterization of γ - γ' nickel-based superalloy microstructures. *Mater. Charact.* **2018**, *142*, 492–503. [[CrossRef](#)]
46. Charpagne, M.A.; Billot, T.; Franchet, J.M.; Bozzolo, N. Heteroepitaxial recrystallization observed in René 65™ and Udimet 720™: A new recrystallization mechanism possibly occurring in all low lattice mismatch γ - γ' Superalloys. In Proceedings of the International Symposium on Superalloys, Seven Springs, PA, USA, 11–15 September 2016; pp. 417–426.
47. Yeom, S.J.; Yoon, D.Y.; Henry, M.F. The morphological changes of γ' precipitates in a Ni-8Al (wt pct) alloy during their coarsening. *Metall. Trans. A* **1993**, *24*, 1975–1981. [[CrossRef](#)]
48. Chen, Y.Q.; Francis, E.; Robson, J.; Preuss, M.; Haigh, S.J. Compositional variations for small-scale gamma prime (γ') precipitates formed at different cooling rates in an advanced Ni-based superalloy. *Acta Mater.* **2015**, *85*, 199–206. [[CrossRef](#)]
49. Song, K.; Aindow, M. Grain growth and particle pinning in a model Ni-based superalloy. *Mater. Sci. Eng. A* **2008**, *479*, 365–372. [[CrossRef](#)]
50. Cormier, J.; Milhet, X.; Mendez, J. Effect of very high temperature short exposures on the dissolution of the γ' phase in single crystal MC2 superalloy. *J. Mater. Sci.* **2007**, *42*, 7780–7786. [[CrossRef](#)]
51. Cruz-Fabiano, A.L.; Logé, R.; Bernacki, M. Assessment of simplified 2D grain growth models from numerical experiments based on a level set framework. *Comput. Mater. Sci.* **2014**, *92*, 305–312. [[CrossRef](#)]
52. Burke, J.; Turnbull, D. Recrystallization and grain growth. *Prog. Phys. Met.* **1952**, *3*, 220–292. [[CrossRef](#)]
53. Foiles, S.M. Temperature dependence of grain boundary free energy and elastic constants. *Scr. Mater.* **2010**, *62*, 231–234. [[CrossRef](#)]
54. Humphreys, J.; Rohrer, G.S.; Rollett, A. *Recrystallization and Related Annealing Phenomena*, 3rd ed.; Elsevier: Amsterdam, The Netherlands, 2017.
55. Bernacki, M.; Logé, R.E.; Coupez, T. Level set framework for the finite-element modelling of recrystallization and grain growth in polycrystalline materials. *Scr. Mater.* **2011**, *64*, 525–528. [[CrossRef](#)]
56. Bernacki, M.; Chastel, Y.; Coupez, T.; Logé, R. Level set framework for the numerical modelling of primary recrystallization in polycrystalline materials. *Scr. Mater.* **2008**, *58*, 1129–1132. [[CrossRef](#)]
57. Merriman, B.; Bence, J.K.; Osher, S.J. Motion of multiple junctions: A level set approach. *J. Comput. Phys.* **1994**, *112*, 334–363. [[CrossRef](#)]
58. Zhao, H.K.; Chan, T.; Merriman, B.; Osher, S. A variational level set approach to multiphase motion. *J. Comput. Phys.* **1996**, *127*, 179–195. [[CrossRef](#)]
59. Fausty, J.; Bozzolo, N.; Pino Muñoz, D.; Bernacki, M. A novel level-set finite element formulation for grain growth with heterogeneous grain boundary energies. *Mater. Des.* **2018**, *160*, 578–590. [[CrossRef](#)]
60. Fausty, J.; Bozzolo, N.; Bernacki, M. A 2D level set finite element grain coarsening study with heterogeneous grain boundary energies. *Appl. Math. Model.* **2020**, *78*, 505–518. [[CrossRef](#)]
61. Furstoss, J.; Bernacki, M.; Petit, C.; Fausty, J.; Pino Muñoz, D.; Ganino, C. Full Field and Mean Field Modeling of Grain Growth in a Multiphase Material Under Dry Conditions: Application to Peridotites. *J. Geophys. Res. Solid Earth* **2020**, *125*, e2019JB018138. [[CrossRef](#)]
62. Hallberg, H.; Bulatov, V.V. Modeling of grain growth under fully anisotropic grain boundary energy. *Model. Simul. Mater. Sci. Eng.* **2019**, *27*, 045002. [[CrossRef](#)]
63. Murgas, B.; Florez, S.; Bozzolo, N.; Fausty, J.; Bernacki, M. Comparative study and limits of different level-set formulations for the modeling of anisotropic grain growth. *Materials* **2021**, *14*, 3883. [[CrossRef](#)]
64. Furstoss, J.; Petit, C.; Tommasi, A.; Ganino, C.; Muñoz, D.P.; Bernacki, M. On the role of solute drag in reconciling laboratory and natural constraints on olivine grain growth kinetics. *Geophys. J. Int.* **2021**, *224*, 1360–1370. [[CrossRef](#)]

65. Scholtes, B.; Shakoor, M.; Settefrati, A.; Bouchard, P.O.; Bozzolo, N.; Bernacki, M. New finite element developments for the full field modeling of microstructural evolutions using the level-set method. *Comput. Mater. Sci.* **2015**, *109*, 388–398. [[CrossRef](#)]
66. Shakoor, M.; Scholtes, B.; Bouchard, P.O.; Bernacki, M. An efficient and parallel level set reinitialization method—Application to micromechanics and microstructural evolutions. *Appl. Math. Model.* **2015**, *39*, 7291–7302. [[CrossRef](#)]
67. Sussman, M.; Smereka, P.; Osher, S. A Level Set Approach for Computing Solutions to Incompressible Two-Phase Flow. *J. Comput. Phys.* **1994**, *114*, 146–159. [[CrossRef](#)]
68. Sethian, J.A. A fast marching level set method for monotonically advancing fronts. *Proc. Natl. Acad. Sci. USA* **1996**, *93*, 1591–1595. [[CrossRef](#)]
69. Sethian, J.A.; Vladimirsky, A. Fast methods for the Eikonal and related Hamilton- Jacobi equations on unstructured meshes. *Proc. Natl. Acad. Sci. USA* **2000**, *97*, 5699–5703. [[CrossRef](#)] [[PubMed](#)]
70. Florez, S.; Shakoor, M.; Toulorge, T.; Bernacki, M. A new finite element strategy to simulate microstructural evolutions. *Comput. Mater. Sci.* **2020**, *172*, 109335. [[CrossRef](#)]
71. Scholtes, B.; Shakoor, M.; Bozzolo, N.; Bouchard, P.O.; Settefrati, A.; Bernacki, M. Advances in Level-Set modeling of recrystallization at the polycrystal scale—Development of the Digi- μ software. *Key Eng. Mater.* **2015**, *651–653*, 617–623. [[CrossRef](#)]
72. Ilin, D.N.; Bozzolo, N.; Toulorge, T.; Bernacki, M. Full field modeling of recrystallization: Effect of intragranular strain gradients on grain boundary shape and kinetics. *Comput. Mater. Sci.* **2018**, *150*, 149–161. [[CrossRef](#)]
73. Moës, N.; Béchet, E.; Tourbier, M. Imposing Dirichlet boundary conditions in the extended finite element method. *Int. J. Numer. Methods Eng.* **2006**, *67*, 1641–1669. [[CrossRef](#)]
74. Florez, S.; Alvarado, K.; Muñoz, D.P.; Bernacki, M. A novel highly efficient Lagrangian model for massively multidomain simulation applied to microstructural evolutions. *Comput. Methods Appl. Mech. Eng.* **2020**, *367*, 113107. [[CrossRef](#)]
75. Hitti, K.; Laure, P.; Coupeuz, T.; Silva, L.; Bernacki, M. Precise generation of complex statistical Representative Volume Elements (RVES) in a finite element context. *Comput. Mater. Sci.* **2012**, *61*, 224–238. [[CrossRef](#)]
76. Crompton, J.S.; Hertzberg, R.W. Analysis of second phase particles in a powder metallurgy HIP nickel-base superalloy. *J. Mater. Sci.* **1986**, *21*, 3445–3454. [[CrossRef](#)]
77. Lin, J.; B.Q. Review and analysis of powder prior boundary (PPB) formation in powder metallurgy processes for nickel-based super alloys. *J. Powder Metall. Min.* **2015**, *4*, 1–6. [[CrossRef](#)]
78. Higashi, M.; Kanno, N. Effect of initial powder particle size on the hot workability of powder metallurgy Ni-based superalloys. *Mater. Des.* **2020**, *194*, 108926. [[CrossRef](#)]
79. Tan, L.; He, G.; Liu, F.; Li, Y.; Jiang, L. Effects of temperature and pressure of hot isostatic pressing on the grain structure of powder metallurgy superalloy. *Materials* **2018**, *11*, 328. [[CrossRef](#)] [[PubMed](#)]
80. Wanhong, Y.; Jian, M.; Wuxiang, W.; Jinwen, Z.; Ruifa, Z. Effects of heat treatment on prior particle boundary precipitation in a powder metallurgy nickel base superalloy. *Adv. Perform. Mater.* **1995**, *2*, 269–279. [[CrossRef](#)]
81. Wu, H.; Zhuang, X.; Nie, Y.; Li, Y.; Jiang, L. Effect of heat treatment on mechanical property and microstructure of a powder metallurgy nickel-based superalloy. *Mater. Sci. Eng. A* **2019**, *754*, 29–37. [[CrossRef](#)]
82. Ye, X.; Li, Y.; Ai, Y.; Nie, Y. Novel powder packing theory with bimodal particle size distribution-application in superalloy. *Adv. Powder Technol.* **2018**, *29*, 2280–2287. [[CrossRef](#)]
83. Tan, L.; Li, Y.; Liu, C.; Yang, C.; Ding, H.; Huang, L.; Liu, F.; Qin, Z.; Jiang, L. The evolution history of superalloy powders during hot consolidation and plastic deformation. *Mater. Charact.* **2018**, *140*, 30–38. [[CrossRef](#)]